UNIVERSITY OF CALIFORNIA

Los Angeles

New Resonances, Gratings, and Slow-wave Structures Based on 2D Periodic Structures

A dissertation submitted in partial satisfaction

of the requirements for the degree

Doctor of Philosophy in Electrical Engineering

by

Xiaoqiang Li

2018

ABSTRACT OF THE DISSERTATION

New Resonances, Gratings, and Slow-wave Structures Based on 2D Periodic Structures

by

Xiaoqiang Li
Doctor of Philosophy in Electrical Engineering
University of California, Los Angeles, 2018
Professor Tatsuo Itoh, Chair

Periodic structure is made of a finite or infinite repetition of a unit cell in one, two or three dimensions. It has been intensively investigated in electromagnetics and widely used in metamaterials, metasurfaces, photonic crystals, frequency selective surfaces (FSS), slow-wave structures, diffraction gratings, etc. Metamaterials and metasurfaces are subsets of periodic structures whose unit cell is much smaller than the wavelength. By proper design of the sub-wavelength unit cell of a periodic structure, its macro properties can be engineered as we wish. This dissertation introduces three novel devices/phenomena which are based on 2D metamaterials/metasurfaces. This dissertation has three sections.

In section I, a new resonance phenomenon is demonstrated in waveguide cavities, which simultaneously uses two orthogonal modes (polarizations). This resonance is formed by bouncing waves with similar handedness, between two simple anisotropic metasurfaces having a relative rotation angle. The tilted anisotropic metasurfaces can cross-couple the waves from one polarization to the other at the cavity end. The field profile of the resonant mode does not exhibit nodes and antinodes, thus the resonant frequency is not solely determined by the cavity length. The resonance condition is theoretically demonstrated from both field and transmission-line perspectives, and is validated by simulations showing the existence of the new resonance. The concept is experimentally demonstrated in an X-band dual-mode circular waveguide, demonstrating a very short cavity resonance. The concept brings new

possibilities for resonator design with size and tunability benefits at different frequencies.

In section II, a metasurface diffraction grating for circularly polarized (CP) incident wave operating at 10 GHz is introduced. Such structure can provide strong auto-collimation for the CP incident wave. Unlike the conventional scatterer, which would typically reverse the handedness of the incident CP wave upon reflection, the proposed grating can preserve the handedness. strong auto-collimation blazing effect and handedness preservation are achieved with specially designed reactive impedance surface, which allows independent control of the responses to transverse electric (TE) and transverse magnetic (TM) polarization. Simulation and measurement are carried out to demonstrate such effect, and comparison with conventional sawtooth grating is made.

In section III, a novel slow-wave substrate integrated waveguide (SIW) is proposed and investigated. The slow-wave effect is achieved by the enhanced capacitance between the signal trace grid and periodic grounded patches on the same top layer. Such slow-wave effect can provide more than 40% size reduction in lateral dimension compared with the conventional SIW with the same cutoff frequency. Meanwhile, the longitudinal dimension can also be reduced by more than 40%. Two-pole bandpass filters (BPF) built from conventional SIW and proposed slow-wave SIW (SW-SIW) are compared through simulations and experiments to demonstrate the applications of our SW-SIW. The BPF implemented with SW-SIW shows a size reduction of 58.8%. Its measured unloaded quality factor (Q_u) is up to 120.2.

The dissertation of Xiaoqiang Li is approved.

Oscar M Stafsudd

Yuanxun Wang

Benjamin S. Williams

Tatsuo Itoh, Committee Chair

University of California, Los Angeles

2018

I would like to dedicate this thesis to my family, especially to my wife, Xuehan Cheng for all her loving support.

TABLE OF CONTENTS

LIST OF FIGURES

LIST OF TABLES

ACKNOWLEDGMENTS

I would like to thank my advisor, Professor Tatsuo Itoh, for his guidance and support on my research and life. None of my research could have been possible without his great mind. I am really proud of being a member of Dragon Gate.

I am also grateful to my committee members, Prof. Oscar M. Stafsudd, Jr., Prof. Yuanxun (Ethan) Wang, and Prof. Benjamin S. Williams, for their time and effort on reviewing my Ph.D. work. Their valuable comments inspired my a lot. I am also grateful to Professor Lijun Jiang, for his kind help on my research.

I would also like to thank Zhi Shen, Lingnan Song, and Botian Zhang. We came to UCLA at the same time, and we are the four guys who took all the electromagnetic courses together since EE 260A. I will never forget the time we spend together.

I would like to express my gratitude to my lab mates, Kirti Dhwaj, Hanseung Lee, Mohammad Memarian, Yasuo Morimoto, Zhi Shen, Haozhan Tian, Riccha Tripati, and Amogh Waghmare, for all the good time we had together. Specially for Kirti Dhwaj, since we spent 4 years together in the lab, and we know each other too well. And of course, I would like to thank all my friends in the nearby labs (there are too many!). You made this place full of happy memories.

In addition, I want to say thank you to Lu Zheng and Professor Xufei Wang. They had tremendous influence on me when I was an undergraduate student. I might have been living a totally different life had I not met them.

Most importantly, I would like to thank my parents and my wife, for their unconditional support. They are the reason why I keep trying for being a better man.

CURRICULUM VITAE

2010 – 2014	B.S. in Physics, Fudan University, Shanghai, China.
2014 – 2016	M.S. in Electrical Engineering, University of California, Los Angeles (UCLA).
2016 – 2018	Ph.D. in Electrical Engineering, University of California, Los Angeles (UCLA).
2017	Finalist for Student Paper Competition International Microwave Symposium 2017, USA
2017	Finalist for Advanced Practice Paper Competition International Microwave Symposium 2017, USA
2018	Nomination for EuMC-2018 Young Engineer Prize European Microwave Conference 2018, Spain

PUBLICATIONS

Li, Xiaoqiang, Mohammad Memarian, and Tatsuo Itoh. "A New Cavity Resonance Assisted by Anisotropic Metasurfaces." IEEE Transactions on Microwave Theory and Techniques (2018).

Li, Xiaoqiang, Kirti Dhwaj, and Tatsuo Itoh. "Single-Layer Slow-Wave Substrate Integrated Waveguide with Enhanced Capacitance." In 2018 IEEE/MTT-S International Microwave Symposium-IMS, pp. 316-318. IEEE, 2018.

Dhwaj, Kirti, **Xiaoqiang Li**, Lijun Jiang, and Tatsuo Itoh. "Low Profile Diplexing Filter/Antenna Based on Common Radiating Cavity with Quasi-Elliptic Response." IEEE Antennas and Wireless Propagation Letters (2018).

Li, Xiaoqiang *et al.* "Resonant blazed metasurface gratings." In Microwave Conference (EuMC), 2018 48th European, pp. 133-136. IEEE, 2018.

Li, Xiaoqiang, *et al.* A new resonance in a circular waveguide cavity assisted by anisotropic metasurfaces. In IEEE MTT-S Int. Microw.Symp., Honolulu, HI, USA, Jun. 4-9 2017.

Memarian, Mohammad, **Xiaoqiang Li**, Yasuo Morimoto, and Tatsuo Itoh. "Wide-band/angle blazed surfaces using multiple coupled blazing resonances." Scientific Reports 7 (2017): 42286.

Morimoto, Yasuo, Mohammad Memarian, **Xiaoqiang Li**, and Tatsuo Itoh. "Open-End Microstrip Line Terminations Using Lossy Gray-Scale Inkjet Printing." IEEE Transactions on Microwave Theory and Techniques 65, no. 12 (2017): 4861-4870.

Li, Xiaoqiang *et al.* Blazed metasurface grating: The planar equivalent of a sawtooth grating. In IEEE MTT-S Int. Microw.Symp., San Francisco, CA, USA, May. 22-27 2016

Dhwaj, Kirti, **Xiaoqiang Li**, Zhi Shen, and Shihan Qin. "Cavity resonators do the trick: A packaged substrate integrated waveguide, dual-band filter." IEEE Microwave Magazine 17, no. 1 (2016): 58-64.

Memarian, Mohammad, **Xiaoqiang Li**, and Tatsuo Itoh. "Resonant blazed metasurface gratings." In Microwave Conference (EuMC), 2016 46th European, pp. 297-300. IEEE, 2016.

Li, Xiaoqiang, Zheng Lu, and Wang Xu-Fei. "In Vivo Magnetic Particle Targeting by Local Gradient Field of Interstitial Seeds Magnetized in an Ex Vivo Uniform Field." Chinese Physics Letters 31, no. 2 (2014): 024701.

CHAPTER 1

A New Cavity Resonance Assisted by Anisotropic Metasurfaces

1.1 Introduction

The conventional standing wave exhibit nodes and anti-nodes regardless of whether it is the result of two counter propagating linearly polarized (LP) waves or two circularly polarized (CP) waves of opposite handedness. By placing different boundary conditions, i.e. short (electric walls) at the nodes, and open (magnetic walls) at the anti-nodes along the axis of propagation, resonant cavities can be formed (Fig. 1.1). These conditions require the cavity length to be integer multiples of quarter wavelength [1–4].

It is proposed in a recent study that a chiral handedness preserving mirror may help to break the cavity length rule for CP plane-waves (PWs) [5]. While a conventional mirror will reverse the handedness of a CP PW incident upon reflection, the chiral mirror will preserve the handedness. The superposition of two counter-propagating CP PWs with the same handedness, leads to a constant amplitude standing wave, termed as the polarization standing wave (PSW) in [6]. With the absence of nodes and anti-nodes in PSWs, the cavity length can be arbitrarily reduced, as long as the two end walls are appropriately chosen to meet the boundary conditions of the PSW. This is a similar end-result as the zeroth order CRLH resonator [7, 8] concept. The PSW concept is a rather interesting and new topic of investigation which utilizes both field polarizations. Refs [5] and [6] only theorized the PSW concept for counter-propagating plane-waves of similar handedness, thus proposing a theoretical Fabry-Perot type cavity with such concept. In addition,they utilized chiral 2D

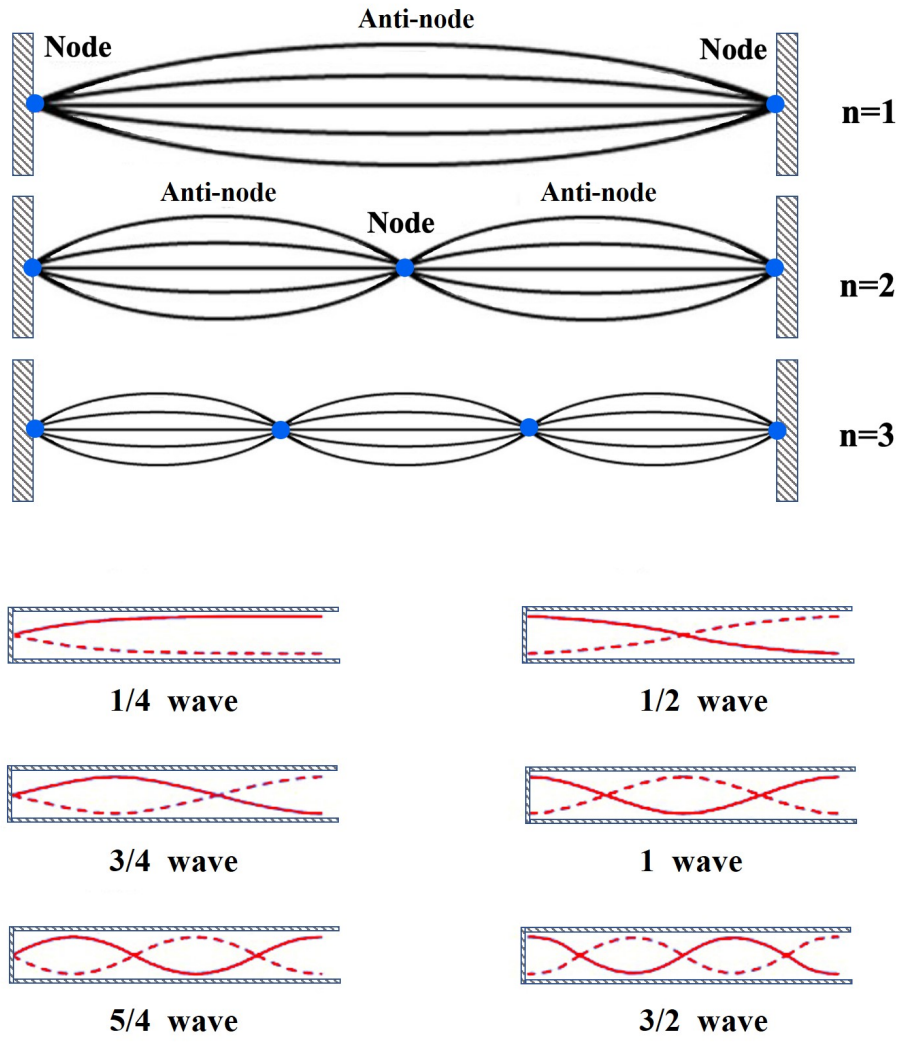

Figure 1.1: Conventional standing waves

surfaces in their designs to preserve the handedness of the CP waves upon reflection. Lastly the overall resonance condition for such a standing wave was not formulated and no resonant cavity (Fabry-Perot type or other) using the PSW was experimentally demonstrated.

In this work [9], we expand our initial results of [10] and present a theoretical solution to this new resonance condition using both a field analysis approach, as well as a transmission-line model. A simple network justification to the resonance phenomenon is provided using the latter approach. The new resonance is then shown to be established by assistance of simple anisotropic boundary condition placed at the cavity ends to serve as handedness preserving reflection surfaces. The handedness preserving reflectors are realized with anisotropic meta-surfaces with relative rotational offset. Each surface provides a perfect electric conductor (PEC) type reflection for one field polarization, while providing a perfect magnetic conductor (PMC) type reflection for the orthogonal field polarization. Therefore such boundaries are termed as PEC-PMC metasurface. It is seen that by proper relative rotation of axis between the two anisotropic end walls, the cavity can resonate at the desired frequency regardless of the cavity length. The dispersion of the metasurfaces are analyzed to investigate the tun-ability of the resonance frequency. To verify the theoretical solutions, full-wave eigenmode simulations are performed. The concept of the new resonance is then extended to guided waves and waveguide resonators. The PEC-PMC metasurfaces are placed as two end walls of a circular waveguide cavity. This leads us to demonstrate, for the first time, a new resonance condition in a dual-mode circular waveguide cavity, which has not been observed before in such structures. Simulation and experimental results demonstrate the validity of the new resonance.

1.2 Analysis for Resonance Conditions

A handedness preserving mirror can be implemented by utilizing a basic property of CP Plane Waves. Any CP PW can be decomposed into two equal amplitude orthogonal LP PWs with a $\pm 90^{\circ}$ phase difference (in phasor form), where the sign determines the handedness based on the propagation direction. An electric wall, such as a metal reflector, reverses the

handedness of an incident CP PW upon reflection, as it is isotropic and provides the same π reflection phase for the two orthogonal LP wave components. Any other isotropic surfaces have similar handedness reversing behavior.

On the other hand, an anisotropic PEC-PMC wall can preserve the handedness upon reflection. LP waves with electric field polarized along the PEC axis, undergo a π radian reflection phase. Whereas the other orthogonal polarization sees a PMC behavior at the surface, and undergoes a 0 radian reflection phase. Upon reflection of a CP wave from such a surface, the sign of the phase difference is reversed and thus the handedness is preserved. Other anisotropic surfaces can also act as handedness preserving mirrors as long as they can provide a π radian reflection phase difference between the two orthogonal axis. Thus, if a CP wave incidents on a handedness preserving mirror, the reflected CP wave shall have the same handedness as the incident CP wave, therefore forming the PSW. Utilizing such handedness preserving surfaces, we can establish a resonant cavity which simultaneously uses both field polarization (in the case of PWs) or both orthogonal guided modes (in a dual mode waveguide). The plane wave (infinite cross section) cavity case is first discussed for simplicity, and then extended to guided modes.

The resonant cavity scenario of interest is presented in Fig. 1.2(a). The cavity axis, and therefore the direction of wave propagation is the z-axis, and the electric field can take any polarization in the $x-y$ plane. One anisotropic end-wall is placed at $z=0$ whose PMC axis is parallel to the $x-$axis while its PEC axis is parallel to the $y-$axis. The second end-wall is placed at $z=L$. The PEC-PMC axes of the second wall are tilted by an angle θ around the z-axis with respect to the first metasurface. Since the PEC-PMC metasurface is rotationally symmetric around the z-axis by every 180°, the value of the tilt angle θ can only be $0 \leq \theta \leq \pi$. A 1D Fabry-Perot type cavity can be formed between these PEC-PMC end-walls, which are infinite in size in the $x-y$ plane. We pursue the eigen-solutions to resonances in such a 1D cavity (along z), where the two surfaces can have arbitrary rotational offset with respect to each other.

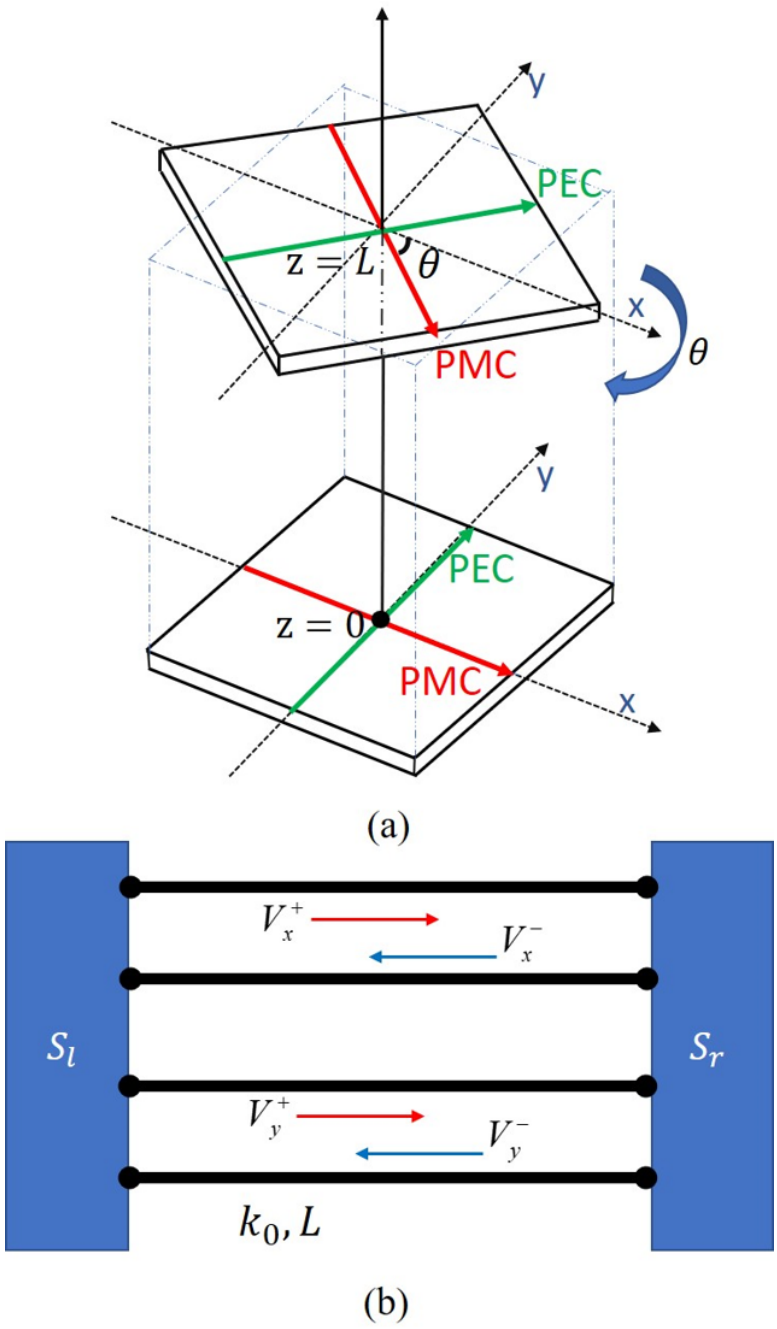

Figure 1.2: (a) A cavity formed with two PEC-PMC anisotropic walls at the two ends. The axes of the wall at $z = L$ are rotated by θ with respect to the first wall. (b) Equivalent transmission line model of the cavity. The two pair of transmission lines represent the two polarizations. The reflecting metasurfaces are equivalent to two-port networks characterized by a 2×2 S-matrix.

1.2.1 Field Analysis Approach

The allowable resonant modes in such a structure may be investigated from two perspectives. The first perspective is to use a field analysis approach [10]. The boundary conditions at the anisotropic surfaces are crucial. The PEC axis boundary condition requires the total tangential E field to be zero along that axis, while the PMC axis boundary condition requires that the maximum tangential E field at the surface to be in this direction. In the case where the anisotropic surface is designed to be PEC-PMC, the boundary condition can be written as:

$$P\hat{E}C \cdot \vec{E}_t = 0 \tag{1.1}$$

$$P\hat{M}C \times \vec{E}_t = 0 \tag{1.2}$$

Since the PEC axis is orthogonal to the PMC axis, (1.1) and (1.2) are effectively equivalent to each other. In other words,the total tangential E field must only exist along the PMC axis at the surface, which makes the total tangential E field perpendicular to the PEC axis.

Now consider the cavity as shown in Fig.1.2. Suppose that both polarizations can exist in the cavity, i.e. the x and y polarization. The general field inside the cavity is

$$\vec{E}_x(z) = \hat{x}(Ae^{-jk_0z} + Be^{+jk_0z}) \tag{1.3}$$

$$\vec{E}_y(z) = \hat{y}(Ce^{-jk_0z} + De^{+jk_0z}) \tag{1.4}$$

where A, B, C, D are the complex amplitudes of the corresponding PWs, and k_0 is the wavenumber of the PWs propagating in free space between the end walls. Applying boundary condition (1.1) to the field at $z = 0$ (the left wall), the relationship between the coefficients are established

$$A = B, \quad C + D = 0 \tag{1.5}$$

Thus the field in the cavity can be rewritten as

$$\vec{E}_x(z) = 2A\cos(k_0 z)\hat{x} \tag{1.6}$$

$$\vec{E}_y(z) = -2jC\sin(k_0 z)\hat{y} \tag{1.7}$$

At $z = L$, due to the rotational offset of the surface, the direction of the PEC axis is

$$P\hat{E}C = \hat{x}\sin\theta + \hat{y}\cos\theta \tag{1.8}$$

Applying the boundary condition (1.1) at $z = L$

$$A\cos(k_0 L)\sin\theta = jC\sin(k_0 L)cos\theta \tag{1.9}$$

Equation (1.9) is the general solution to the resonance in this cavity. One possible and somewhat intuitive solution to (1.9) would be $\theta = 0$ or $\pi/2$, along with a second condition on $k_0 l$ which make both sides equal to zero. When $\theta = 0$, $\sin\theta = 0$, and the left-hand side of (1.9) equals to zero. To satisfy the right-hand side of (1.9) we have,

$$\sin(k_0 L) = 0 \Rightarrow k_0 L = n\pi, (n = 0, 1, 2, \cdots) \tag{1.10}$$

When $\theta = \pi/2$, $\cos\theta = 0$ and the right-hand side of (1.9) equals to zero. In this case, we need

$$\cos(k_0 L) = 0 \Rightarrow k_0 L = n\pi + \frac{\pi}{2}, (n = 0, 1, 2, \cdots) \tag{1.11}$$

Therefore in both cases, we obtain the solution by forcing one side of (1.9) equals zero by properly setting the rotation angle, and equating the other side to zero by imposing a condition on the cavity length. The two polarizations would decouple, and waves along each polarization would resonate independently in both cases. In other words, there is no interaction between the two polarizations in the cavity. These two scenarios correspond to the classic resonances in a 1D cavity. For each polarization, the case of $\theta = 0$, corresponds to the case where either both ends of the cavity are short (PEC) or both are open (PMC). The case of $\theta = \pi/2$ corresponds to the so called half-mode resonances, where one cavity end

is PEC and the other is PMC for one polarization, and vice versa for the other polarization. These classic modes can resonate independently from the other polarization.

However, magic happens when θ takes any other value aside from 0, π. The field of the two polarizations cannot be decoupled and θ cannot be eliminated in such scenario. Another solution to (1.9) may be obtained by assuming

$$A = \pm jC \tag{1.12}$$

This is essentially assuming that the PWs traveling in the cavity are CP type, where one polarization is equal and in quadrature phase with respect to the other polarization. Such assumption is based on the knowledge that PSW is essentially formed by two counter-propagating CP wave with the same handedness. Substitute (1.12) in (1.9), we obtain

$$\sin(k_0 L)\cos\theta \mp \cos(k_0 L)\sin\theta = \sin(k_0 L \mp \theta) = 0 \tag{1.13}$$

Clearly, the solution to (1.13) is a new resonance condition where

$$k_0 L \mp \theta = n\pi, (n = 0, 1, 2, \cdots) \tag{1.14}$$

One immediate observation is that the resonance condition is not only dependent on $k_0 l$ but also on values of θ between 0, π. The relationship also depends on the handedness of the CP wave. It also suggests a potential tunability of the resonance frequency by rotating the surface instead of changing the cavity length. Higher order resonances of order $n > 0$ are also possible.

If we apply the assumption (1.12) in (1.6) and (1.7), the total field in the cavity can be rewritten as

$$\vec{E}_t(z) = 2jC(\pm\cos(k_0 z)\hat{x} - \sin(k_0 z)\hat{y}) \tag{1.15}$$

therefore

$$|E_t(z)| = 2C \tag{1.16}$$

which shows that the amplitude of the total E field is constant along the z-direction and no nodes and anti-nodes are present. It should also be noted that the direction of the E field

at any given z is

$$Angle(z) = \arctan \frac{E_y(z)}{E_x(z)} = \mp k_0 z \tag{1.17}$$

which has a linear dependency on z. It shows that the tip of the E field vector follows a helical path around z-axis. In addition, the direction of the E field is only dependent on z given the frequency. The features of this field distribution fits the PSW profile [6].

Researchers have tried to break the cavity size limitation in the past by placing metafilms in Fabry-Perot cavities [11, 12]. While such resonance conditions as proposed in [11] seem to have a similar format with (14), the principles behind them are quite different. In [11, 12], classic linearly polarized resonances were used. The metafilm behaves as a L-C network providing additional phase as if there were an additional length of a transmission line. This is similar to using shunt lumped L-C elements in a microstrip resonator to decrease the resonance frequency. Their approach works for either eigen-polarizations independently in the Fabry-Perot Cavity, and is utilizing the traditional resonances (i.e. the two polarizations are not coupled to form a new resonance). However, in PSW resonance, the two eigen-polarizations in the Fabry-Perot Cavity must be related together to form such a new standing wave without nodes and anti-nodes. The rotation angle of the end walls here will provide the additional phase. In addition, their approach does not provide tunability since the topology of the metafilm decides the resonance frequency for a given cavity. It would demand changing the geometry of the metafilm to change the resonance frequency without changing the cavity size. On the other hand, we only need to rotate the anisotropic surface to tune our new resonance.

The field analysis approach provides an efficient and intuitive way for the analytical solution to the resonance condition of PSW. However, the solution is not exclusive. We manually imposed (1.12) and reached a solution. As much plausible as the assumption (1.12) might be, one may argue that there could be other modes aside from the aforementioned three types of modes based on the different relationship of A and C in (1.9). For example, assume A and C also have a magnitude difference

$$A = \pm jCM \tag{1.18}$$

Now (1.9) can be rewritten as

$$\tan(k_0 L) = \pm M \tan\theta \tag{1.19}$$

Eq. (1.19) results in a new resonance condition where the magnitude ratio between each polarization also comes into the picture. In this scenario, the field is like PSW except that it has an elliptically polarized nature. However, a few problems arise from this result. The first is that there would be infinitely many modes for a given configuration of the cavity and a given frequency, due to infinitely many possible different magnitude ratios between A and C, which seems impossible. The second is that this mode cannot be captured by full wave simulation tools, which make its existence even more questionable. In addition, the field perspective cannot be used to analyze the cases other than the PEC-PMC anisotropic surface scenario. The answer to these questions can be easily seen from a circuit perspective.

1.2.2 Transmission Line Model Analysis

It is natural to take the x and y polarization LP waves as a set of eigen-polarizations for the 1D propagation since the resonance is caused by the PWs bouncing back and forth between the two walls. Any PWs that propagates along z can therefore be interpreted as a linear superposition of the two eigen-polarizations. Note that there is no energy coupling between the two eigen-polarization PWs in free space (unless this region is filled with a chiral material itself [13], which is not the case here). Fig. 1.2(b) shows a network representation of the scenario at hand with such perspective. The free-space propagation path between the two end walls is equivalent to a two transmission-line network. Each transmission-line corresponds to one eigen-polarization with a propagation constant equal to k_0 for free space. The end walls are modeled as four-port networks responsible for reflections and transmissions on both polarizations. In the most general case, the matrix representation of scattering from

a discontinuity in the propagation path of a two-transmission line system is:

$$\begin{bmatrix} b_{1x} \\ b_{1y} \\ b_{2x} \\ b_{2y} \end{bmatrix} = [S] \begin{bmatrix} a_{1x} \\ a_{1y} \\ a_{2x} \\ a_{2y} \end{bmatrix}$$

where

$$S = \begin{pmatrix} s_{1x1x} & s_{1x1y} & s_{1x2x} & s_{1x2y} \\ s_{1y1x} & s_{1y1y} & s_{1y2x} & s_{1y2y} \\ s_{2x1x} & s_{2x1y} & s_{2x2x} & s_{2x2y} \\ s_{2y1x} & s_{2y1y} & s_{2y2x} & s_{2y2y} \end{pmatrix} \tag{1.20}$$

Here $1x$ and $1y$ notations denote the x- and y-polarization scatterings on the left side of the discontinuity, and $2x$ and $2y$ for the right side. In the particular discontinuity of Fig. 1.2(b), there are only reflections and no transmission. Therefore, only one side of the surface is of interest. The scattering matrix of each surface can then reduce to a two-port network where only the reflected fields on the same side are of interest:

$$\begin{bmatrix} V_x^- \\ V_y^- \end{bmatrix} = [S] \begin{bmatrix} V_x^+ \\ V_y^+ \end{bmatrix}$$

where

$$S = \begin{pmatrix} s_{xx} & s_{xy} \\ s_{yx} & s_{yy} \end{pmatrix} \tag{1.21}$$

The equivalent transmission-line model of the dual-polarized cavity and the reflection discontinuities are given in Fig. 1.2(b). Since the circuit model can describe the end-walls by using the scattering matrix, it is not required for the end-wall to be PEC-PMC anisotropic surface for the deduction. Any handedness preserving mirror can be used as the reflector for this problem. The scattering matrix describing this reflector is

$$S_l = \begin{pmatrix} e^{j\phi} & 0 \\ 0 & -e^{j\phi} \end{pmatrix} \tag{1.22}$$

The end-well degenerates into PEC-PMC anisotropic surface when $\phi = 0$.

However, the scattering matrix for the right wall is not as straightforward. The principal axes of this wall have a rotation around the z-axis, by an amount θ. The scattering matrix of the right wall S_r, defined in the $x-y$ coordinate system, can be obtained by the coordinate transformation of S_l using the rotation matrix $R(\theta)$:

$$S_r = R(\theta) S_l R(\theta)^T = \begin{pmatrix} e^{j\phi}\cos 2\theta & e^{j\phi}\sin 2\theta \\ e^{j\phi}\sin 2\theta & -e^{j\phi}\cos 2\theta \end{pmatrix} \tag{1.23}$$

where

$$R(\theta) = \begin{pmatrix} \cos\theta & -\sin\theta \\ \sin\theta & \cos\theta \end{pmatrix} \tag{1.24}$$

Now consider the resonance path. The plane waves in $+z$ direction from $z = 0$ reach $z = L$ and are reflected by the second end-wall, then travel in z direction, are reflected by the first end-wall at $z = 0$, and reach their initial position. Assuming everthing is lossless.the resonance requires that the wave and all its derivatives be continuous after this one round-trip. Letting E_1 and E_2 represent the initial complex amplitude of the two eigen-polarization PWs, the described resonance round-trip can be written in matrix form as:

$$\begin{aligned} &\begin{pmatrix} e^{j\phi} & 0 \\ 0 & -e^{j\phi} \end{pmatrix} \begin{pmatrix} e^{j\phi}\cos 2\theta & e^{j\phi}\sin 2\theta \\ e^{j\phi}\sin 2\theta & -e^{j\phi}\cos 2\theta \end{pmatrix} \begin{pmatrix} E_1 \\ E_2 \end{pmatrix} \\ &\cdot e^{-2jk_0 l} = \begin{pmatrix} E_1 \\ E_2 \end{pmatrix} e^{j2m\pi}, (m = 0, 1, 2, \cdots) \end{aligned} \tag{1.25}$$

Rearranging equation (1.25) we have

$$\begin{pmatrix} \cos 2\theta & \sin 2\theta \\ -\sin 2\theta & \cos 2\theta \end{pmatrix} \begin{pmatrix} E_1 \\ E_2 \end{pmatrix} = e^{j2(m\pi + k_0 l - \phi)} \begin{pmatrix} E_1 \\ E_2 \end{pmatrix} \tag{1.26}$$

Denote the left-most matrix of (1.26) as A. It can be observed that $e^{j2(m\pi+k_0 l)}$ is the eigen-value, and $(E_1, E_2)^T$ is the eigenvector of A.

When $\theta = 0$, A is an identity matrix whose eigenvalues are $\lambda_1 = \lambda_2 = 1$. In this case,

$$e^{j2(m\pi + k_0 l - \phi)} = 1 \Rightarrow k_0 l = n\pi + \phi, (n = 0, 1, 2, \cdots) \tag{1.27}$$

When $\theta = \pi/2$, A is again an identity matrix with a minus sign. Its eigenvalues are $\lambda_1 = \lambda_2 = -1$. In this scenario,

$$e^{j2(m\pi+k_0l-\phi)} = -1 \Rightarrow k_0l = n\pi + \frac{\pi}{2} + \phi, (n = 0, 1, 2, \cdots) \tag{1.28}$$

The eigenvectors for $\theta = 0$ and $\theta = \pi/2$ are $x_1 = (1, 0)^T$ and $x_2 = (0, 1)^T$ respectively. These eigenvectors indicate that E_1 and E_2 are independent. These two resonances correspond to the classic resonant modes described earlier and agree with the results in (1.10) and (1.11) from the field analysis when $\phi = 0$.

However, A is no longer an identity matrix when θ is any other value. The eigenvectors of A in general can be obtained as

$$x = \begin{pmatrix} \frac{\cos 2\theta \mp 2j \sin\theta\cos\theta - \cos 2\theta}{\sin 2\theta} \\ 1 \end{pmatrix} = \begin{pmatrix} \frac{\mp 2j \sin\theta\cos\theta}{\sin 2\theta} \\ 1 \end{pmatrix} \tag{1.29}$$

which leads to two fixed eigenvectors:

$$x_1 = \begin{pmatrix} j \\ 1 \end{pmatrix}, \quad x_2 = \begin{pmatrix} -j \\ 1 \end{pmatrix} \tag{1.30}$$

This shows that the eigenvectors are independent of the tilt angle θ. More importantly, by using (1.29), the relationship of E_1 and E_2 can be obtained as

$$E_1 = \pm jE_2 \tag{1.31}$$

Eq. (1.30) reveals the circularly polarized nature of the waves inside the cavity at resonance. The sign also indicates the handedness of the CP PWs. In addition, the CP nature is independent of the tilt angle θ. More importantly we have not imposed any presumptions on the PWs in the cavity, yet the CP PWs revealed themselves as the only eigen solutions for resonance as long as $\theta \neq \pi, \pi/2$. The possibility of elliptical PSW is ruled out by this transmission line argument. By solving the matrix, the eigenvalues are $\lambda_1 = e^{-j2\theta}, \lambda_2 = e^{+j2\theta}$. In this case, the resonance condition is

$$\begin{aligned} &e^{j2(n\pi+k_0l-\phi)} = \lambda = e^{\mp j2\theta} \\ &\Rightarrow k_0l = n\pi + \phi \mp \theta, (n = 0, 1, 2, \cdots) \end{aligned} \tag{1.32}$$

which agrees with (1.14) when $\phi = 0$. The total field inside the cavity can be obtained by superposition of the two counter propagating CP PWs of same handedness:

$$\begin{aligned} \overrightarrow{E}_t(z) = \overrightarrow{E}_+(z) + \overrightarrow{E}_-(z) = \begin{pmatrix} E_0 \\ \pm jE_0 \end{pmatrix} e^{-jk_0 z} + \\ S_1^{-1} \begin{pmatrix} E_0 \pm jE_0 \end{pmatrix} e^{+jk_0 z} = \begin{pmatrix} E_0 \cos k_0 z \\ \mp E_0 \sin k_0 z \end{pmatrix} \end{aligned} \tag{1.33}$$

which agrees with (1.15) when $\phi = 0$. The presence of the off-diagonal elements in S_r and thus in A, cause the coupling between the two eigen-polarizations at the cavity ends, and form the new resonance.

1.2.3 Resonance Condition with Dispersion

In reality, the surfaces realizing the handedness preserving boundaries are dispersive over frequency (their reflection phase on the two axises does not necessarily keep the same difference as the frequency changes). When the tuning of the resonance frequency is desired, the dispersion of these metasurfaces is therefore inevitable. Fortunately, the transmission line model can accommodate this. For a PEC-PMC metasurface as example, the wave will see PEC for one polarization for all frequencies. While the wave with the other polarization will see PMC only at the center frequency and deviate on other frequencies [10]. Thus, the scattering matrix can be modified as

$$S_1 = \begin{pmatrix} e^{j\phi(f)} & 0 \\ 0 & -1 \end{pmatrix} \tag{1.34}$$

where ϕ is the reflection angle caused by the dispersion, which is a function of frequency for a given metasurface. The scattering matrix for the second wall can also be obtained by applying the rotation matrix

$$\begin{aligned} S_r &= R(\theta) S_l R(\theta)^T \\ &= \begin{pmatrix} -\sin^2\theta + e^{j\phi(f)}\cos^2\theta & \frac{\sin 2\theta(1+e^{j\phi(f)})}{2} \\ \frac{\sin 2\theta(1+e^{j\phi(f)})}{2} & -\cos^2\theta + e^{j\phi(f)}\sin^2\theta \end{pmatrix} \end{aligned} \tag{1.35}$$

The final equation can be obtained by using the same procedure as in previous sections,

$$\begin{pmatrix} -e^{j\phi(f)}(\sin^2\theta - e^{j\phi(f)}\cos^2\theta) & \frac{\sin 2\theta e^{j\phi(f)}(1+e^{j\phi(f)})}{2} \\ -\frac{\sin 2\theta(1+e^{j\phi(f)})}{2} & \cos^2\theta - e^{j\phi(f)}\sin^2\theta \end{pmatrix} \cdot \begin{pmatrix} E_1 \\ E_2 \end{pmatrix} = e^{j2(m\pi+k_0 l)} \begin{pmatrix} E_1 \\ E_2 \end{pmatrix} \tag{1.36}$$

This is again an eigenvalue problem where the eigenvalues can be calculated

$$\begin{aligned} \lambda &= e^{j\phi(f)}(\cos^2\theta + \cos\phi(f)\cos^2\theta - 1) \\ &\mp \cos\tfrac{\phi(f)}{2} e^{j\phi(f)} \cos\theta \sqrt{2(\cos^2\theta + \cos^2\theta\cos\phi(f) - 2)} \end{aligned} \tag{1.37}$$

Thus the resonance condition can be numerically written as

$$\lambda - e^{j2k_0 l} = 0 \tag{1.38}$$

Equation (1.38) is a function of cavity length l, the tilt angle θ and resonance frequency f. The analytical solution is not obvious, yet the graphical method can be employed by plotting the curve where

$$\left|\lambda - e^{j2k_0 l}\right| = 0 \tag{1.39}$$

From (1.39), the resonance frequency can be obtained once the cavity length and the rotation angle is given. It would allow the precise tuning over a large frequency band with realistic metasurface designs.

1.3 Design and Validation

To verify the above theory and solutions, full-wave simulations are performed on cavities formed with the realistic handedness preserving surfaces of the PEC-PMC metasurface type. Many studies have demonstrated PMCs in microwaves and optics [14–19]. However, they are not all compatible with an anisotropic PEC-PMC feature. Studies on anisotropic metasurfaces are also widely investigated [20–24]. However, they are either complex to fabricate or too hard to obtain PEC-PMC characteristics. In this paper, a novel and simple PEC-PMC

metasurface design at 10 GHz is utilized. We demonstrated in [25] that sub-wavelength periodic parallel metal traces on a grounded substrate respond differently to orthogonal polarizations. This structure is a planar implementation of the artificial soft and hard surface, which is typically implemented with 3D corrugated structures [26]. Such a structure is shown in Fig. 1.3a. If the incident E field is parallel to the traces, denoted as the TE mode, the surface behaves as a PEC. If the E field is perpendicular to the metal traces, denoted as TM mode, it acts as an reactive impedance surface whose refection phase can be designed. Therefore, we can obtain an anisotropic PEC-PMC surface by simply designing the TM reflection phase to be 0 radians at the center frequency.A unit-cell of the structure used in simulations is shown in Fig. 1.3b. The substrates have a relative permittivity $\epsilon_r = 10.2$ and a thickness $H = 2.22$ mm. The periodicity of the structure is $d = 2.25$ mm. The strip width w is to be optimized to implement a proper reflection phase.

Fig. 1.3c shows the reflection phase for both TE and TM mode over $4 - 16$ GHz when strip width $w = 0.75$ mm. It can be observed that the reflection phase is 0.205°for TM mode and 174.5° for TE mode at 10 GHz. The results indicate that the surface behaves as an almost perfect PMC for TM mode at 10 GHz. For TE mode, since the electric field sees a dense array of metal strips and some effects of dielectric, the reflection phase is not exactly π radians instead of a solid metal surface. This concludes the design of the PEC-PMC anisotropic boundary condition, using a very simple metasurface. It should be noted that although an empirical method based on simulation of the reflection phase was used to design the desired strip width, relatively accurate circuit models[27] may also have been used to reach the same result.

1.3.1 Validation for Free Space

Full-wave eigenmode simulations are then carried out for a cavity constructed with two of such anisotropic metasurfaces placed at some distance apart. As shown in Fig.1.4, the cavity is formed by placing two PEC-PMC metasurfaces in parallel with a distance L in the z-direction . Such a cavity is periodic in the transverse $x - y$ plane and thus has infinite

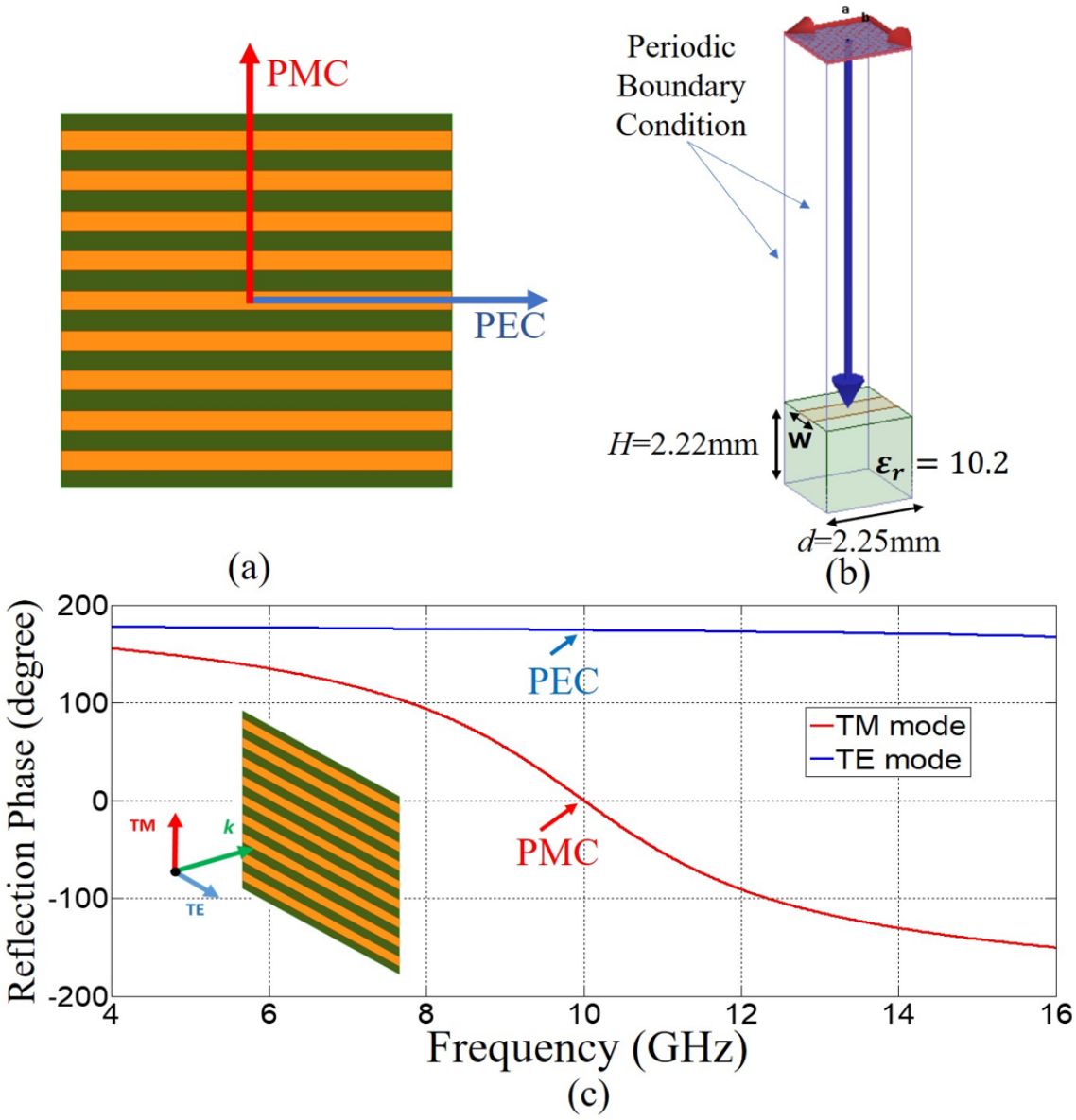

Figure 1.3: (a) Proposed PEC-PMC anisotropic metasurface structure. (b) the unit cell simulation of the metasurface. Floquet port is deembeded to the surface of the metal strips. (c) the reflection angle over 4-16 GHz.

transverse cross-section. In the cases shown in Fig. 1.4, the rotation angle θ between the two end walls can either be 0 or $\pi/2$ radians. The periodic boundary condition is employed to mimic the infinite PEC-PMC surface and the infinite cavity cross section.

According to (1.10) and (1.27), the resonance will occur at 10 GHz by setting $l = 15$ mm and $\theta = 0$. Moreover, there are two possible resonances that can be captured. One resonance is a PEC-PEC type and the other is for a PMC-PMC type. That is indeed the case from the simulation results. Fig. 1.4a shows the former type of resonance which has E field nodes (short circuit) on the two end walls and one anti-node in the center, with the resonance frequency $f_1 = 9.71$ GHz. The field only has one polarization which is parallel to the PEC axis. Fig. 1.4b shows the other type of resonance which has E field anti-nodes on the two end walls (open circuit) and one node in the center. The field only has one polarization which is parallel to the PMC axis. The resonance frequency is exactly 10 GHz.

According to (1.11) and (1.28), a half-mode resonance should also occur at 10 GHz by letting $l = 7.5$ mm and $\theta = 90°$. As in previous discussions, the field would meet the PEC boundary condition at one end and PMC boundary condition at the other end thus forming a half-mode resonator. This is exactly the situation shown in Fig. 1.4c. The maximum field at one end along the PMC axis and the minimum field at the other end along the PEC axis. The resonance frequency is 9.92 GHz.

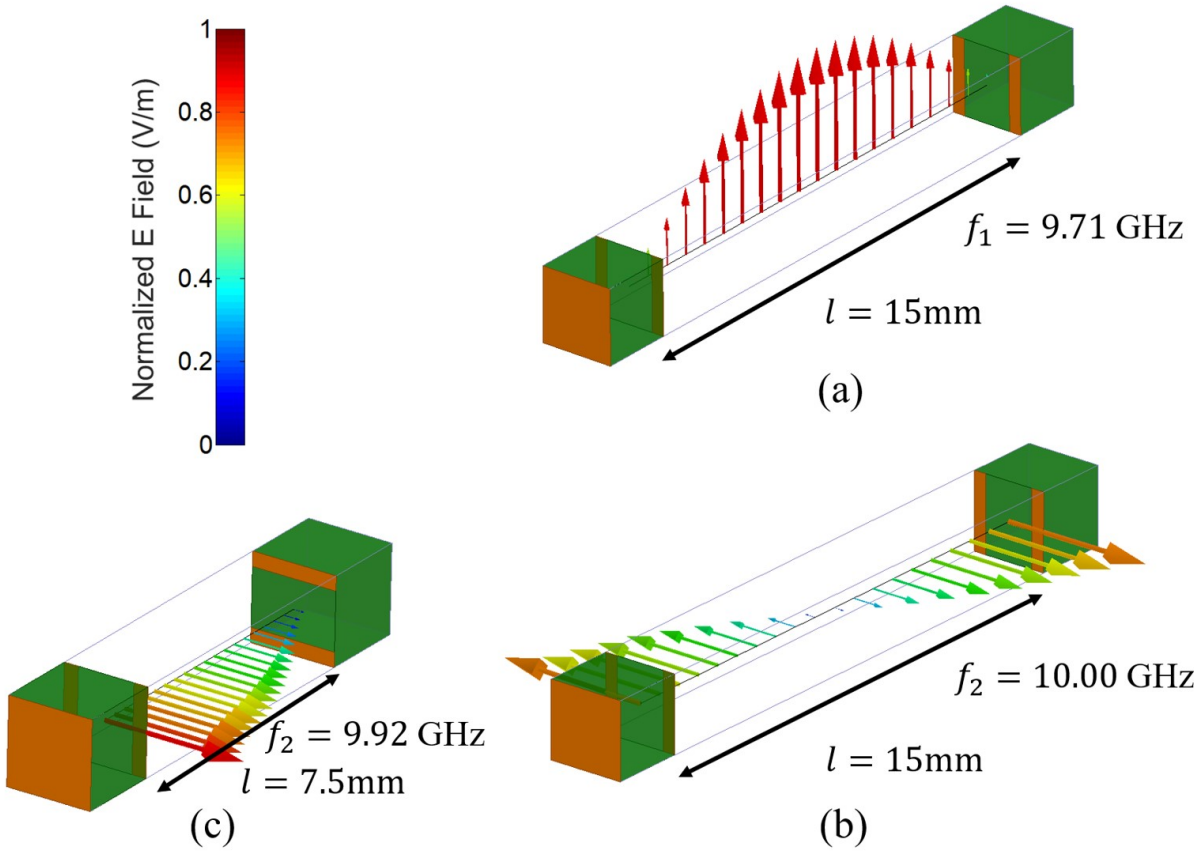

Figure 1.4: Eigenmode simulations of a cavity with independent resonances on each polarization. (a) When $l = 15$ mm and $\theta = 0$, the eigen-mode have nodes on the two end walls and one anti-node in center. The resonance frequency $f_1 = 9.71$ GHz. (b) When $l = 15$ mm and $\theta = 0$, the eigenmode have anti-nodes on the two end walls and a node in center. The resonance frequency $f_2 = 10.00$ GHz. (c) When $l = 7.5$ mm and $\theta = 90°$, the eigenmode shows the maximum field at one end along the PMC axis and the minimum field at the other end along the PEC axis. The resonance frequency $f_3 = 9.92$ GHz.

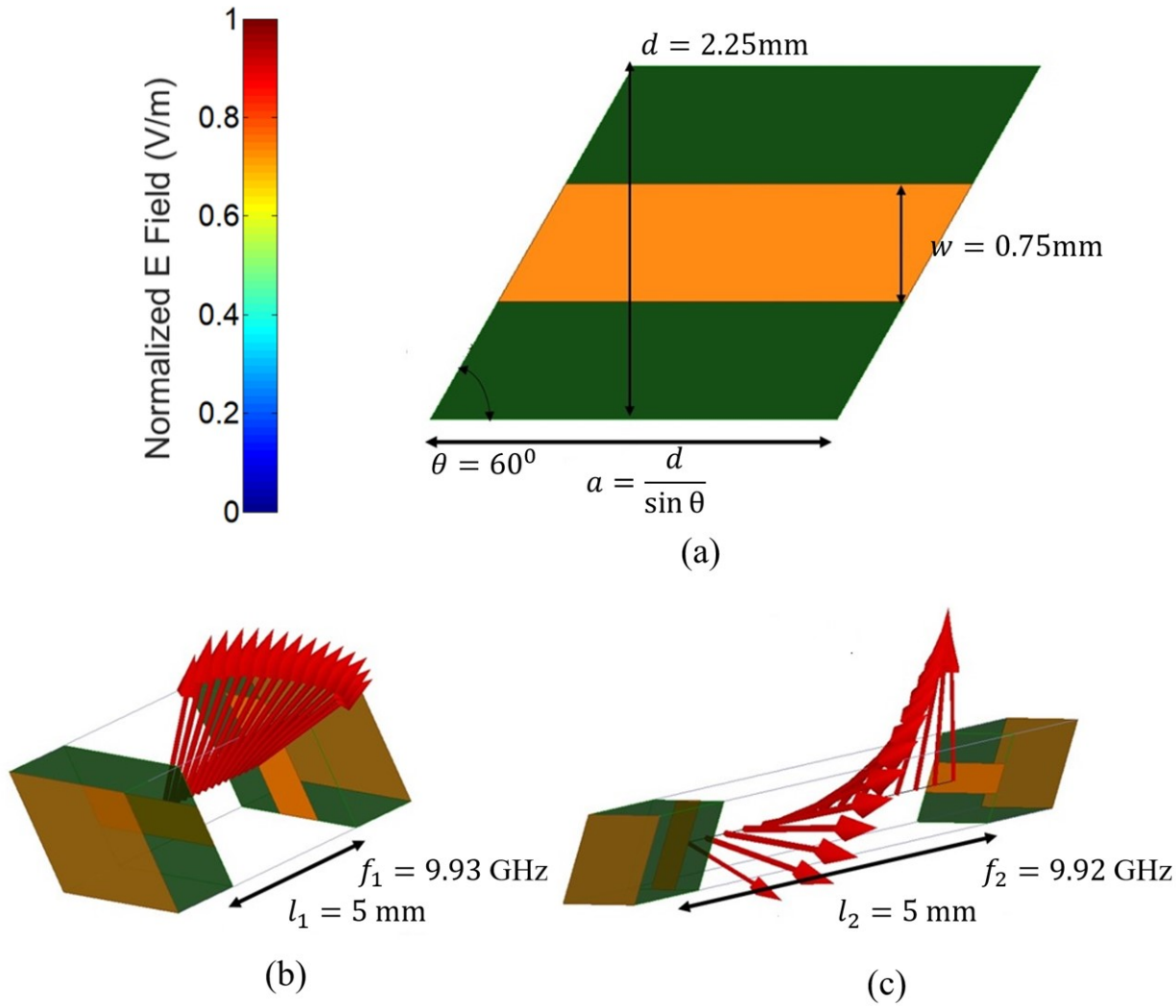

Figure 1.5: Eigenmode simulations when the two surface have arbitrary rotation angle. (a) Rhombus unit cell of the metasurfaces to form a cavity for $\theta = 60°$ and $120°$ rotation. (b)the rotation angle between the two end walls $\theta_1 = 60°$ and the distance $l_1 = 5$ mm. The eigenmode fields have constant field amplitude and a helix profile. The tip of the E field rotates $60°$ from one end wall to the other. The resonance frequency $f_1 = 9.93$ GHz. (c) the rotation angle between the two end walls $\theta_2 = 120°$ and the distance $l_2 = 10$ mm. The eigenmode field have constant field amplitude and a helix profile. The tip of the E field rotates $120°$ from one end wall to the other. The resonance frequency $f_2 = 9.92$ GHz.

What the previous simulations described is simply nothing but the classic resonances typically seen in 1D cavities with short or open ends. To verify the resonance conditions (1.14) and (1.32), eigenmode simulations are required where the two end walls have other relative rotation angles with respect to each other. As presented in Fig. 1.5a, a rhombus unit-cell is used to implement the rotation angle θ. The rotation angle $\theta = 60°$ and $120°$ are chosen for demonstration. The rhombus cell is only chosen to accommodate the rotation angle between the two parallel metasurfaces in the context of an eigenmode simulation of the full cavity and they exactly recover the same metasurface as in Fig. 1.3a.

As shown in Fig. 1.5b and 1.5c, two periodic PEC-PMC metasurfaces are placed parallel with a distance of $l_1 = 5$ mm and $l_2 = 10$ mm respectively to form a cavity. The rotation angle between the principal axes of the two end walls are $\theta_1 = 60°$ and $\theta_2 = 120°$ respectively.

According to (1.14) and (1.32), the resonance frequency will be 10 GHz when $l_1 = 5$ mm for $\theta_1 = 60°$ (Fig. 1.5b) and $l_2 = 10$ mm for $\theta_2 = 120°$ (Fig. 1.5c). That is indeed the case. For the former scenario, the resonance frequency $f_1 = 9.93$ GHz and for the latter scenario, a resonance frequency $f_2 = 9.92$ GHz are observed in the full-wave eigenmode simulations. The field along the main axis of the cavity has uniform amplitude in both cases. The tip of the electric field forms a helical path and it rotates 60° and 120° respectively from one end wall to the other. The direction of the electric field at a given point does not rotate with time. The direction which E-field oscillates along is determined by the position and frequency. The field profile exactly fits the descriptions in (1.15) (1.17) and (1.33).

1.3.2 Validation for Free Space Considering Dispersion

As we mentioned, the metasurface will deviate from PEC-PMC response when the frequency is off from the center frequency. In this case, the aforementioned graphic solution in (1.34)-(1.39) can be used. The relationship between reflection phase and frequency of the metasurface shown in Fig. 1.3c within 8-12 GHz can be approximated by using linear curve fitting as

$$\phi(f) = c_1 f + c_2 \tag{1.40}$$

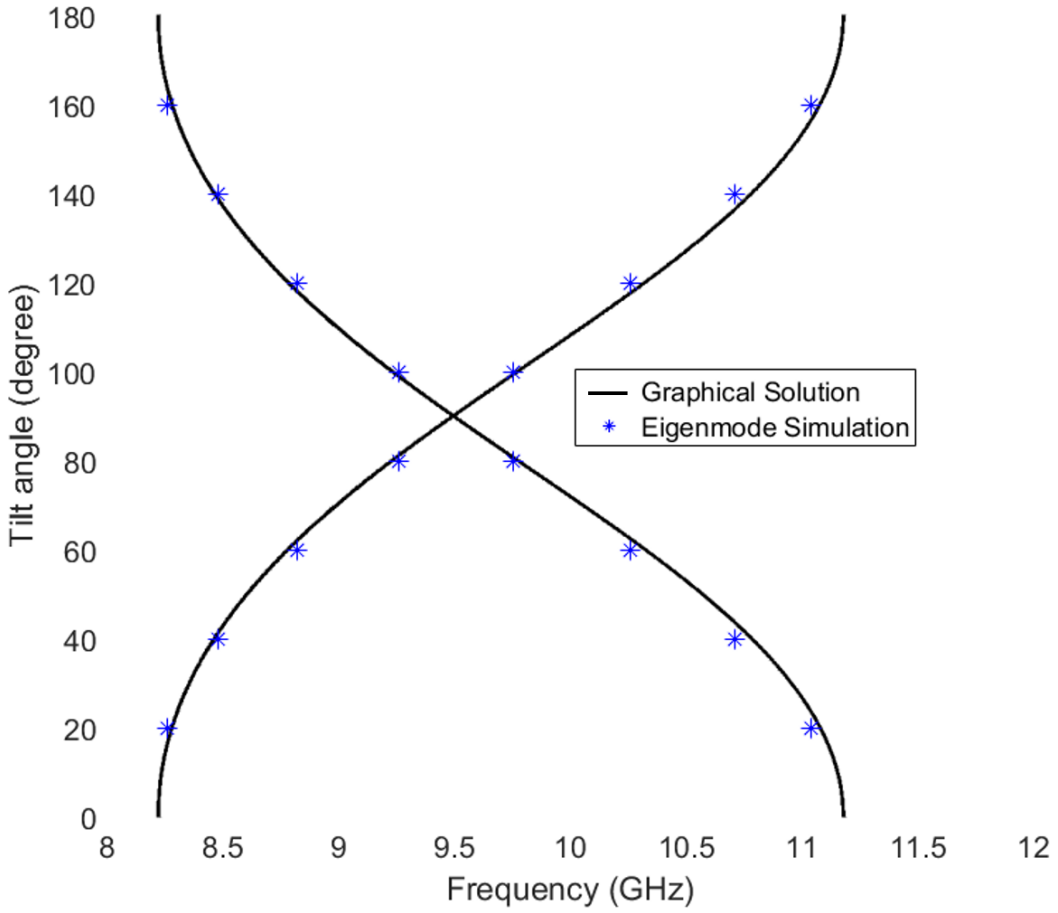

Figure 1.6: Graphical solution and the eigenmode simulation results. The cavity length $l = 9$ mm.

where $c_1 = -50.04\ ^o/\text{GHz}$ and $c_2 = -500.08^o$.

In real application scenario, the cavity length is fixed while the rotation angle of the end wall will be changed for tuning. Thus the cavity length is set to be $l = 9$ mm for demonstration. The unit cell presented in Fig. 1.5a is employed to simulate the cases where the rotation angle θ equals to 20°, 40°, 60° and 80°. The symmetry of the metasurface implies that these cases are equivalent to 160°, 140°, 120°, and 100° respectively. The result from the eigenmode simulation and the graphical solution from the modified transmission line model are shown in Fig. 1.6. The simulated results perfectly fit the graphic solution from (1.39).

1.4 New Resonance in Dual-Mode Waveguide Cavities

The previous discussions covered a resonance for plane-waves with an infinite transverse area. However, this resonance condition inspires us to seek a similar resonance condition in closed guided-wave cavities. Unlike PWs, waves in waveguides are not infinite and uniform in their transverse plane, and they typically follow a sinusoidal variation. However, many waveguides, such as dual-mode waveguides, can simultaneously support two orthogonal modes, having two E fields polarized orthogonal to each other in the transverse plane. An experiment using a dual-mode circular waveguide cavity is carried out for demonstration of the new resonance and verification of the theoretical solution, as shown in Fig. 1.7.

The circular waveguide is made of a copper tube with an inner diameter $D = 25.27$ mm. Two PEC-PMC anisotropic metasurfaces using the similar design as in Fig. 1.3a are placed at the two ends of the waveguide. Rogers RT/duroid 6010LM with dielectric constant $\epsilon_r = 10.2$ at 10 GHz and thickness $h = 1.91$ mm is used to implement the surfaces. A relative rotation angle between the two surfaces is set as $\theta = 135°$.

It has to be noted the excitation of a such resonance is rather simple even though the new resonance has CP nature. It does not require two orthogonal probes with 90° phase delay to enforce the CP wave inside the cavity. As we presented in the early sections, the new

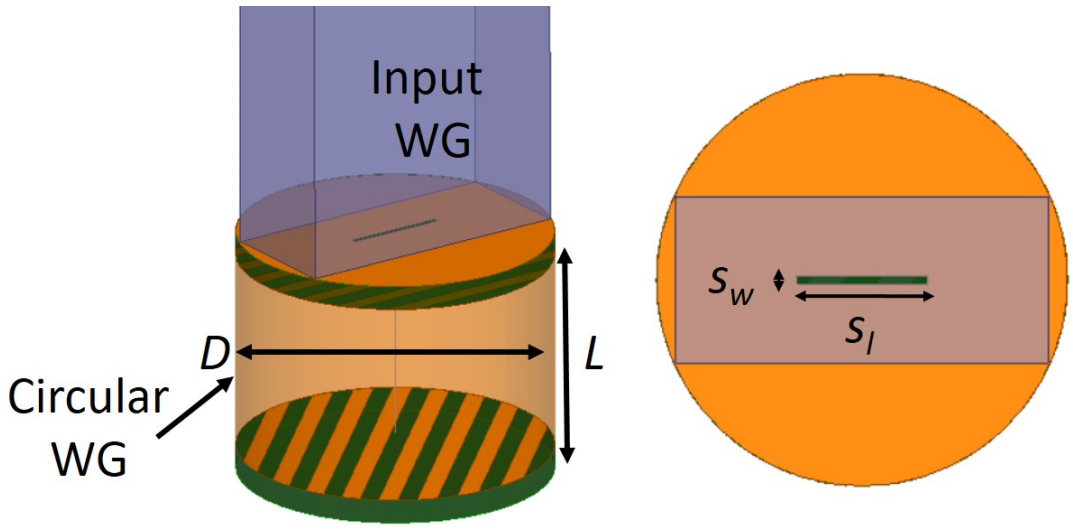

Figure 1.7: A circular waveguide cavity with PEC-PMC end walls excited with a standard waveguide through a coupling slot.

resonance is an eigenmode of the cavity. As long as the power is properly coupled into the cavity, the new resonance mode can be excited. In this demonstration, the cavity is excited by a standard WR-90 rectangular waveguide through a coupling slot with dimension $s_l = 8$ mm by $s_w = 0.5$ mm. The coupling slot is etched on the ground back of the metasurface that joins the input WR-90 WG to the cavity. The slot also acts as polarizing the field along the particular PMC direction.

We still have two orthogonal polarizations of the guided TE_{11} modes of the circular waveguide cavity While we do not deal with CP plane waves anymore. These two modes can be made to have $\pm 90°$ phase difference, and thus represent a similar type of handed propagation. This is particularly applicable to the center axis of the guide along the z-axis, where the TE_{11} mode has a strong and uniform distribution. The guided wave number β for TE_{11} mode in this waveguide is [3]

$$\beta = \sqrt{{k_0}^2 - \frac{\chi'_{11}}{D/2}} \tag{1.41}$$

The cavity length L can be obtained by using (1.14) or (1.32) to design the $n = 0$ order

resonance frequency to be at 10 GHz for a rotation angle of $\theta = 135°$,

$$L = \frac{\theta}{\beta} = 15.84 \text{ mm} \tag{1.42}$$

The reason why $\theta = 135°$ was chosen in our prototype instead of $\theta = 45°$ is to have a larger device that can be built and measured more easily. According to (1.14) or (1.32), if $\theta = 45°$, the cavity length L would be 5.28 mm. It must be noted that these cavity lengths do not correspond to cavity lengths of any resonant orders of a conventional TE_{11} metallic dual-mode waveguide cavity of the same cross section.

The resonant structure is 3D, rather than the one-dimensional plane wave discussion in previous discussions and [6]. To verify that the resonance is the one theorized, we carry out full-wave simulations of the entire structure with no periodic conditions. Fig. 1.8a shows the field inside the circular cavity along the center z-axis for the resonance frequency. The E field vector follows a helical path with about 135° total rotation, and relatively uniform amplitude. Closer observation shows that the field at the two end boundaries are aligned with the PMC axis. These features meet the desired field profile described in (1.16) (1.17) (1.33), but now for a guided wave.

A more complete field distribution within the cross section is given in Fig. 1.8b. We can see that the electric field is very close to the TE_{11} mode in the circular wave guide. The mode profile is perturbed at the end walls. The metasurface is designed to have a PEC axis and PMC axis. However, the electric field of TE_{11} mode in the circular cavity is not uniform on the whole transverse plane. Therefore, at the metasurface, the direction of the E field varies with the position and sees different reflection coefficients. That causes the deformation of the mode. Nevertheless, the E field of TE_{11} mode in the vast center part is relatively strong and uniform, which enables us to approximate the field inside to be a PW and apply the previous theory. Though the field near the side wall is more distorted, the magnitude of these field and the area it possesses is too small to significantly affect the overall field compared with the field in the center. It can also be observed that the polarization of the perturbed TE_{11} mode rotates based on their locations along the z-axis, which is the same as the rotation of the E field polarization in (1.16) (1.17) (1.33). A series of simulations of the cavity structure

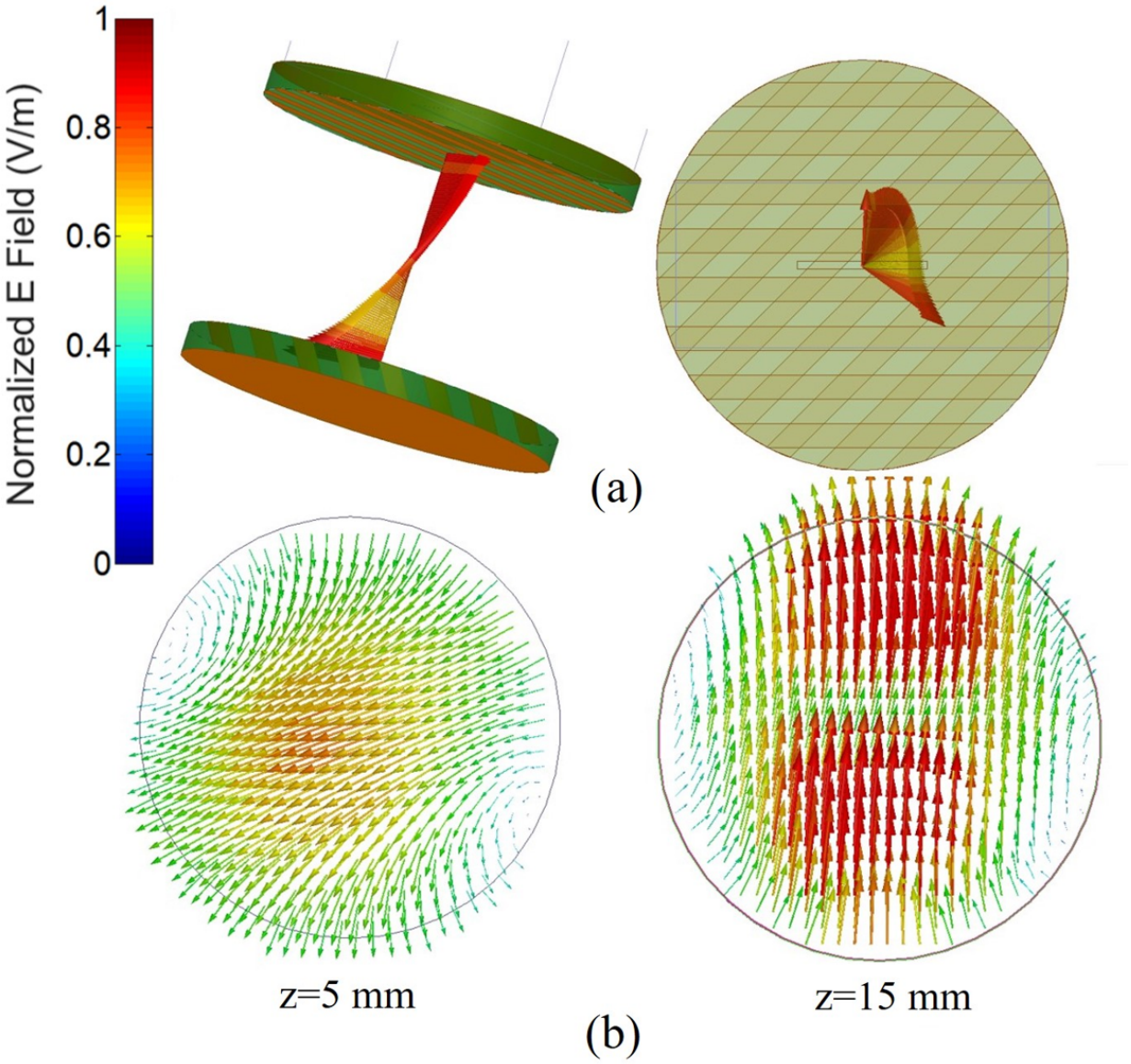

Figure 1.8: Electric field in the circular cavity at resonance. (a) The E field along the center line. (b) The E field in the cross sections of the cavity. The field is very close to TE_{11} mode profile in different polarizations based on their positions.

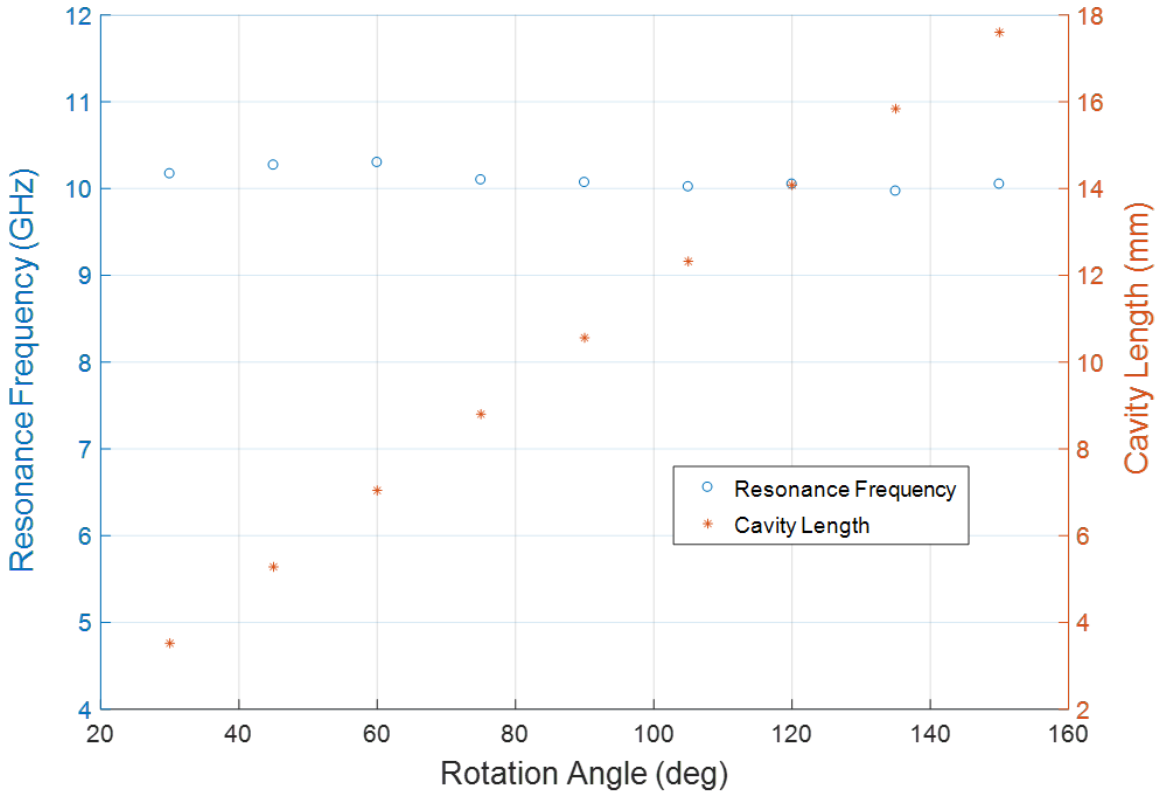

Figure 1.9: The resonance frequencies under different combinations of cavity lengths and rotation angles

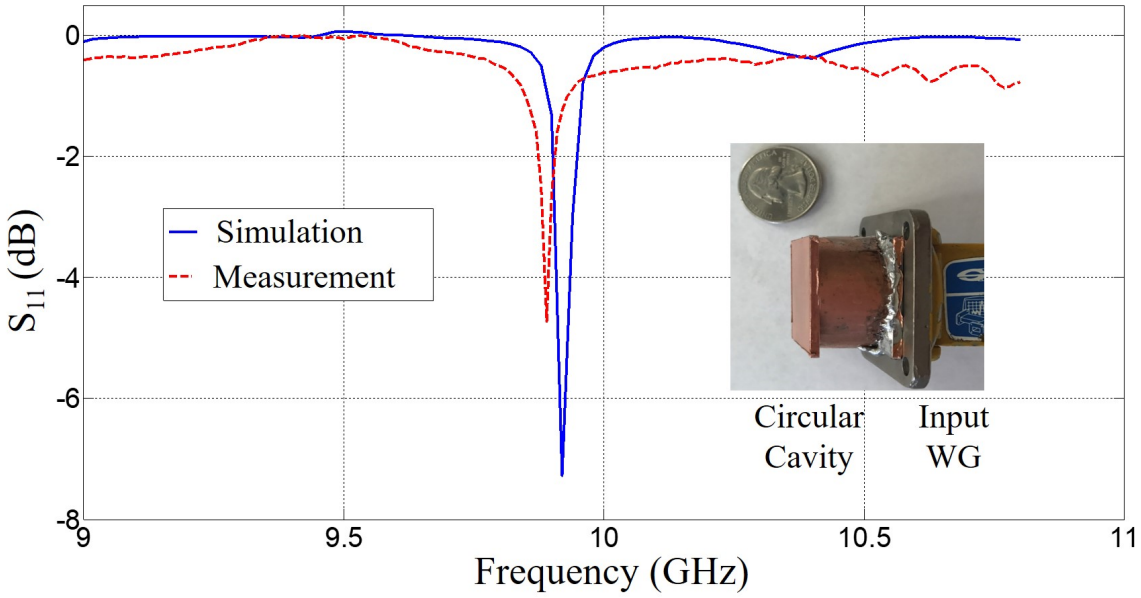

Figure 1.10: Measured and simulated S-parameters showing a new resonance at 10 GHz for a dual-mode wave-guide cavity of length 15.84 mm.

shown in Fig.7 are conducted under different combinations of cavity lengths and rotation angles, to further verify the resonance condition and demonstrate the possibility of the size reduction. The combinations are designed under (1.14) (1.32) (1.42) such that the resonance frequencies shall be at 10 GHz. The results are presented in Fig. 1.9. The metasurfaces used in each case are the same, and only the rotation angle and cavity length is adjusted. It can be seen that as the rotation angle decreases, the required cavity length for the given resonance frequency also decreases.

Fig. 1.10 shows the single port S-parameter of both simulation and measurement of the circular cavity. The simulation result clearly indicates that a resonance occurs at 9.97 GHz. This matches the theoretic prediction perfectly. The measurement also shows the resonance is at 9.89 GHz, which agrees well with the simulation results. We fixed the rotation angle for demonstration for simplicity. However the resonance can be tuned by turning the end walls according to (1.39). This tuning process can be accordingly controlled by a step motors etc., providing a reliable way of tuning the resonance. If the device is big, the rotation can also

be achieved by hand. We are able to achieve both discrete and continuous levels of tuning. This provides a new possibility for tunning the resonance frequencies as opposed to the conventional tunable resonators [28–35], in which the dimensions of the cavities are changed, MEMs switches are used, and tuning screws or liquid metals are inserted. Moreover, one can envision coupling of such resonators, to realize multipole coupled resonator filters [36, 37]. The simulated unloaded quality factor Q_u for this cavity is 590. The major loss comes from the dielectric loss, and conductor loss is also an important source. If an all-dielectric metasurface is employed with very low loss dielectrics[20] or utilize all-metal corrugated structures, the cavity′s Q_u can be improved up to 6000. So that the applications could be extended into optical and THz regime.

1.5 Conclusion

A new resonance is presented in cavities. Such resonance is a result of dual-polarized propagation reflecting from anisotropic boundary conditions that can relate the two polarizations. Two approaches toward the analytical solution of the resonance condition is presented, namely a transmission line model as well as a fields perspective.The dispersion of the end walls are also characterized using the transmission line model. Anisotropic PEC-PMC metasurfaces were employed to implement a handedness preserving reflection surface and used as cavity boundary conditions. The theoretical solution to this resonance was verified using full-wave eigenmode simulations. A new resonance in dual-mode circular waveguide cavities was then reported, and experimentally demonstrated, inspired from the earlier plane wave discussions. This new resonance has potential application in tunable resonator design at microwave, mm-wave and the THz regions.

CHAPTER 2

Blazed Metasurface Grating with Handedness Preservation for Circularly Polarized Incident Wave

2.1 Introduction

Diffraction grating is a periodic structure which can diffract incident wave into different directions (diffraction orders). The diffraction orders are dictated by the frequency and angle of the incident wave, and the periodicity of the gratings [38–43].

For any diffraction grating, the relationship between the operation wavelength λ_0, the periodicity d, the diffraction order m, the incident angle θ_i, and the diffraction angle of the m_{th} order θ_m can be expressed using the grating equation. As shown in Fig. 2.1, the grating equation 2.1 can be obtained by simply regarding the diffraction beams as the consequence of constructive interference.

$$(\sin\theta_i + \sin\theta_m)d = m\lambda \tag{2.1}$$

In the Littrow configuration, the incident angle and the diffraction angle of the $m = -1$ mode are the same, i.e. $\theta_i = \theta_{-1}$. The grating equation can be rearranged as

$$k_0 d \sin\theta_i = \pi \tag{2.2}$$

Eq. (2.2) is also referred to the Bragg condition [39].

Conventional diffraction gratings are typically 3D structure, e.g. sawtooth gratings [38] and groove gratings [39]. These gratings have many applications in optics and microwave. For example, diffraction grating can be used in tunable external-cavity diode lasers [44]. As

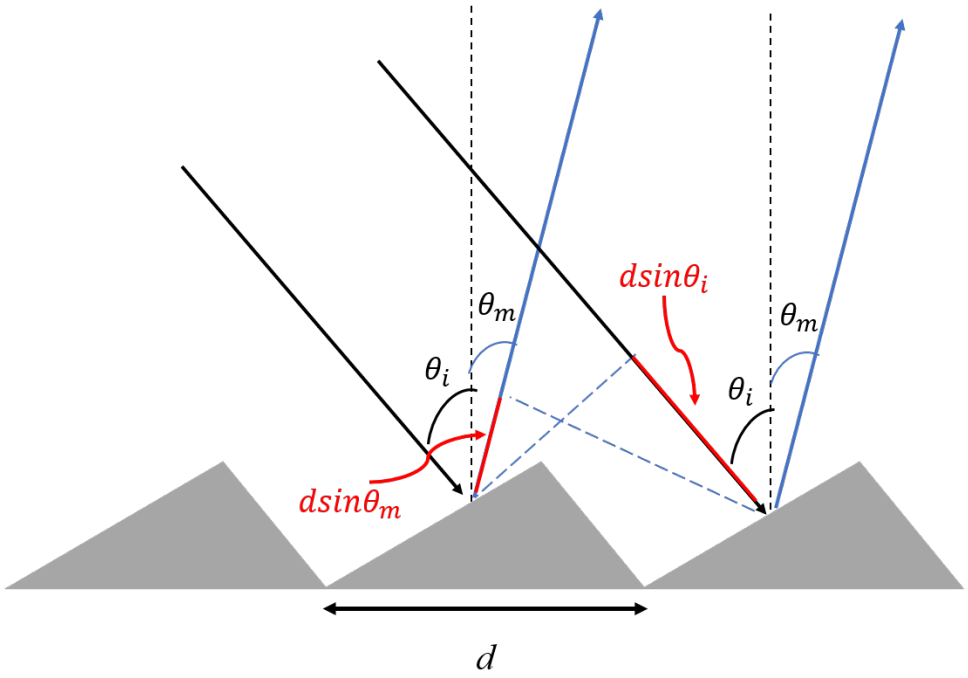

Figure 2.1: Illustration of a diffraction grating.

illustrated in Fig. 2.2, the diffraction grating acts as an output coupler. $m = -1$ mode is coupled back to the cavity whereas the specular reflection ($m = 0$ mode) forms the output beam.

However, 3D structures can be difficult and expensive to fabricate. In addition, it is hard for these 3D structures to provide independent control over different polarizations. Therefore, alternative approaches are sometimes desired. Metasurfaces [43] are planar periodic structures which allow people to engineer its properties, e.g. the local magnitude and phase of reflection/transmission coefficients of the surface. Such technology can be employed to manipulate the scattered wave front, thus can serve as the planar equivalent of a 3D diffraction gratings. There are several metasurface gratings that have been proposed recently. In [25], a metasurface grating is proposed to replace a sawtooth grating in Littrow configuration for TE polarization by reproduce the phase distribution of the scattered field of a sawtooth grating. Similar approach is used in [45–47] to operate on both TE and TM polarizations simultaneously. In [48–51], resonant type blazed metasurface gratings are proposed to achieve

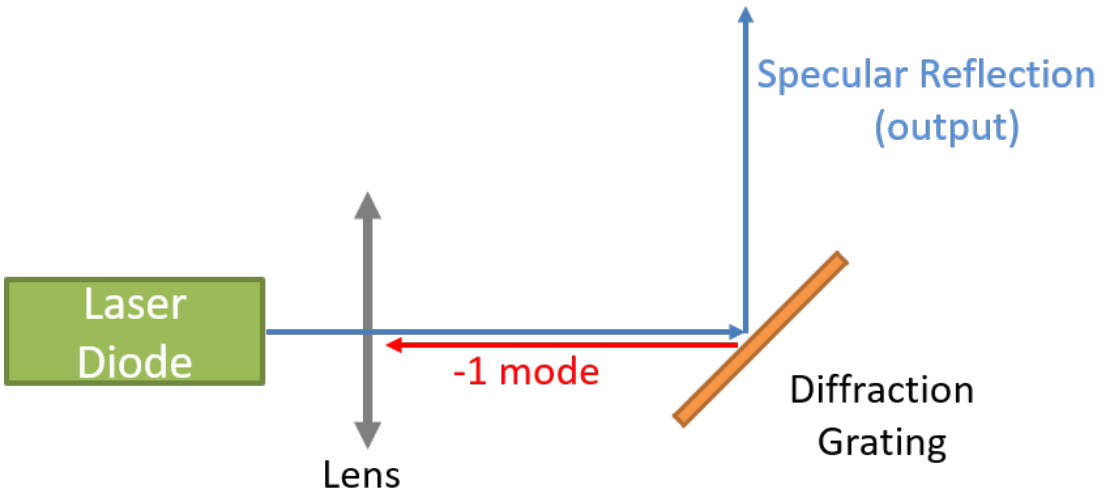

Figure 2.2: Illustration of a tunable external-cavity diode laser.

strong auto-collimation in TM polarization. Meanwhile, non-periodic metasurface which can create strong retro reflection in TE polarization is investigated in [52, 53] by using genetic algorithm for optimization.

Nevertheless, to our best recollection, there has been no diffraction grating, either metasurface grating or classic 3D grating, reported to operate on CP incident wave and can preserve the handedness. However, such diffraction grating is desired if we would like to use it into an external-cavity diode laser with the new resonance mode that we discussed in chapter 1. In this work [54], we propose a novel metasurface grating operating at 10 GHz, which not only provides strong auto-collimation for CP incident wave, but also preserves the handedness (Fig. 2.3).

2.2 principle of operation

The grating we desire in this work has two features: strong blazing and handedness preservation. We may divide and conquer the problems. First is to achieve strong blazing. As we discussed in previous sections, Bragg condition is needed to achieve the auto-collimation. However, satisfying Bragg condition does not guarantee strong auto-collimation blazing ef-

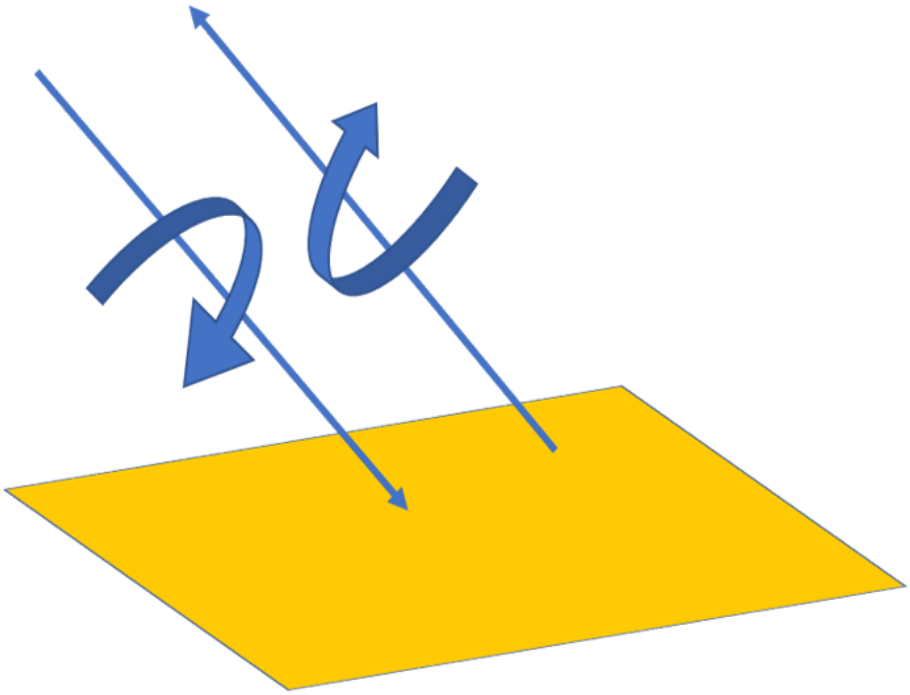

Figure 2.3: Concept of the blazed metasurface grating with handedness preservation for CP incident wave

fect. The properties of the unit-cell is also important. In this project, we propose a novel method to create very strong blazing reflection by putting perfect electric condutor (PEC) and perfect magnetic conductor (PMC) scatters together in one period. An example of incident wave at 10 GHz with incident angle $\theta_i = -30^o$ is shown in Fig. 2.4 to illustrate the concept.

According to Bragg condition, the periodicity of the unit-cell $d = \lambda_0$ in this case. Thus the two scatters (blue for PEC, red for PMC) are placed $\lambda_0/2$ away from each other. It can be readily calculated that the scattered waves from the two scatters in $m = 0$ mode (specular reflection) are in destructive interference, whereas the scattered waves in $m = -1$ mode are in constructive interference. Therefore the specular reflection is suppressed while the $m = -1$ mode is enhanced.

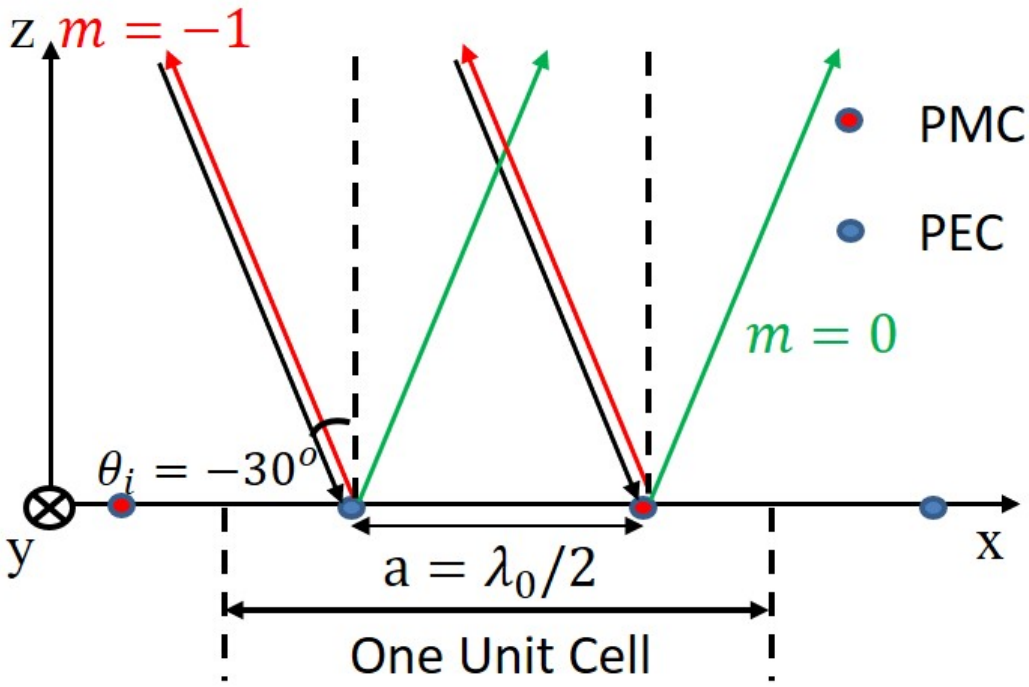

Figure 2.4: Illustration for a unit-cell of the diffraction grating: the incident wave is at 10 GHz, and incident angle is $\theta_i = -30^o$. The blue dot and red dot represent PEC and PMC scatterers respectively.

On the other hand, the handedness preservation requires the unit-cell to provide 180^o degree difference between the reflection phases of TE (E-field in y-direction) and TM (E-field in x-z plane) polarizations, as we discussed in chapter 1. One way to achieve such effect is to let the blue scatter in Fig. 2.4 to behave as PEC for TE wave and PMC for TM wave, and let the red scatter to behave as PEC for TM wave and PMC for TE wave, vice versa. In this way, the TE and TM ploarizations seems opposite boundary conditions and undergo 180^o reflection phase difference with respect to each other.

2.3 Implementation

The idea in previous section can be implemented by strip-type reactive impedance surface. Such surface is similar as the surface we use in chapter 1 for implementing PEC-PMC anisotropic surface. However, the discussion in previous section is based on ideal case, i.e. the PEC and PMC scatters are point sources that are separated $\lambda_0/2$ away. In reality, they are two continuous regions that are distributed in each unit-cell. Therefore many parameters, such as the ratio between two regions and actual reflection phases of PEC/PMC regions, have to be optimized.

Fig. 2.5 shows the proposed structure. The substrate is Rogers RT/duroid 6010 with dielectric constant $\epsilon_r = 10.2$, thickness $h = 1.27$mm, and copper cladding $t_c = 35$um. The period of the unit-cell in x-direction d is chosen to be 30 mm to meet the Bragg condition at 10 GHz and $\theta_i = \theta_{-1} = -30^o$. The period in y-direction $a = 2$mm is chosen for design simplicity. The length of region I is $d_1 = 20$mm, and the copper strip width is $w_1 = 1.85$mm. The length of region II is $d_2 = 10$mm. There are 5 parallel copper strips in y direction, and the width of the strips is $w_2 = 1.82$mm.

We can speculate the responses of two regions for TE and TM polarizations. Region I would behave as PEC for TM wave and PMC for TE wave, whereas region II would behave as PEC for TE wave and PMC for TM wave. This is what we desired as discussed in the previous section.

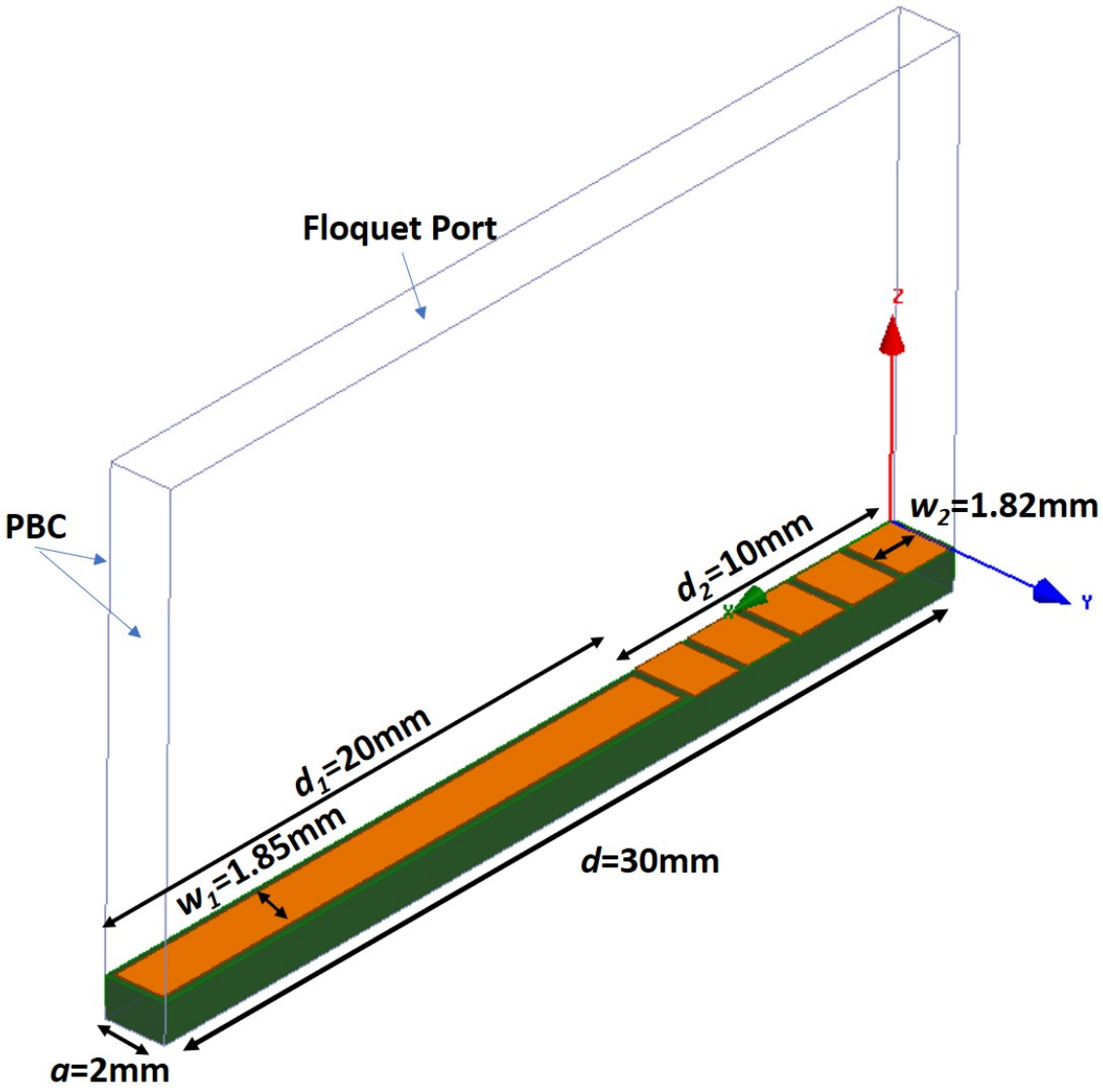

Figure 2.5: Unit-cell of the metasurface grating optimized for auto-collimation at $\theta_i = \theta_{-1} = -30^o$.

Full wave simulation is preformed on this unit-cell with periodic boundary conditions (PBC) and Floquet port. The magnitude and phase of the reflection coefficients for TE and TM polarizations in $m = -1$ mode are shown in Fig. 2.6.

At 10 GHz, the magnitudes of $m = -1$ mode for both TE and TM polarizations are very strong, and their values are close to each other. Meanwhile, the difference of reflection

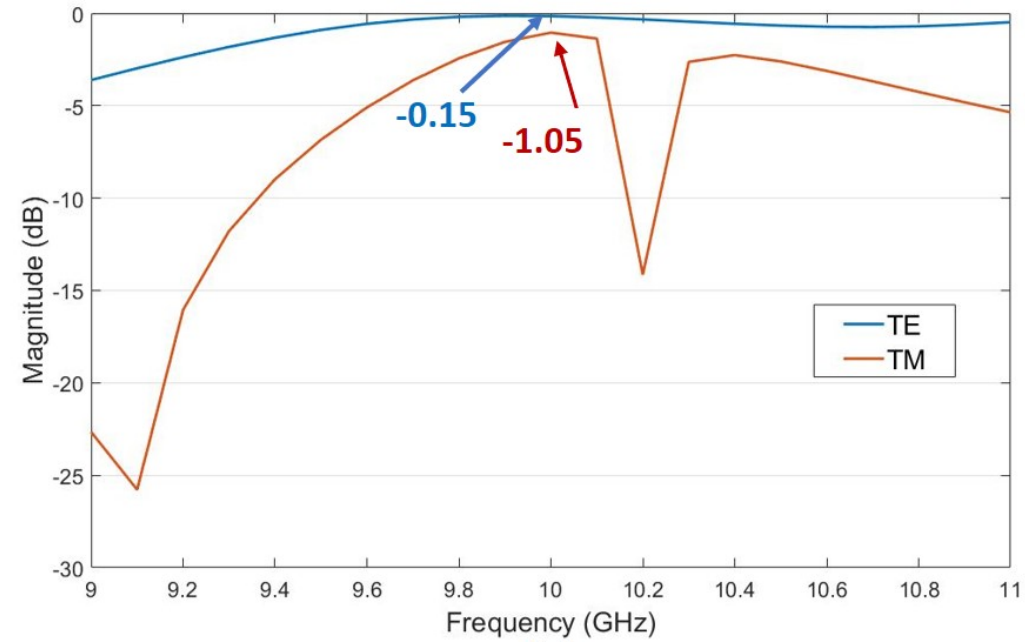

(a)

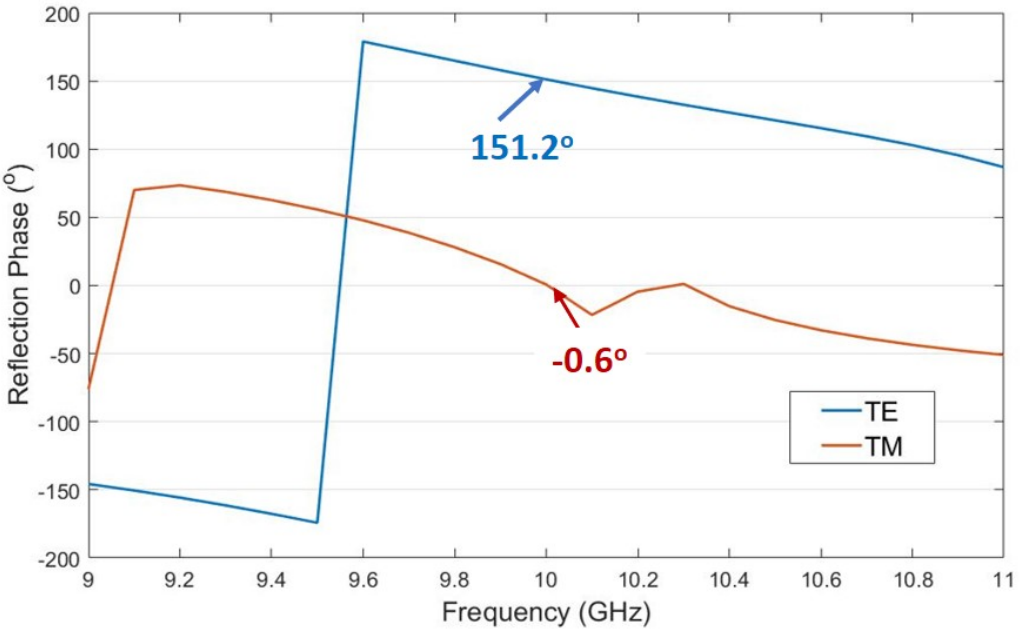

(b)

Figure 2.6: (a) The magnitude of the reflection coefficient for m=-1 mode. (b) The phase of the reflection coefficient for m=-1 mode

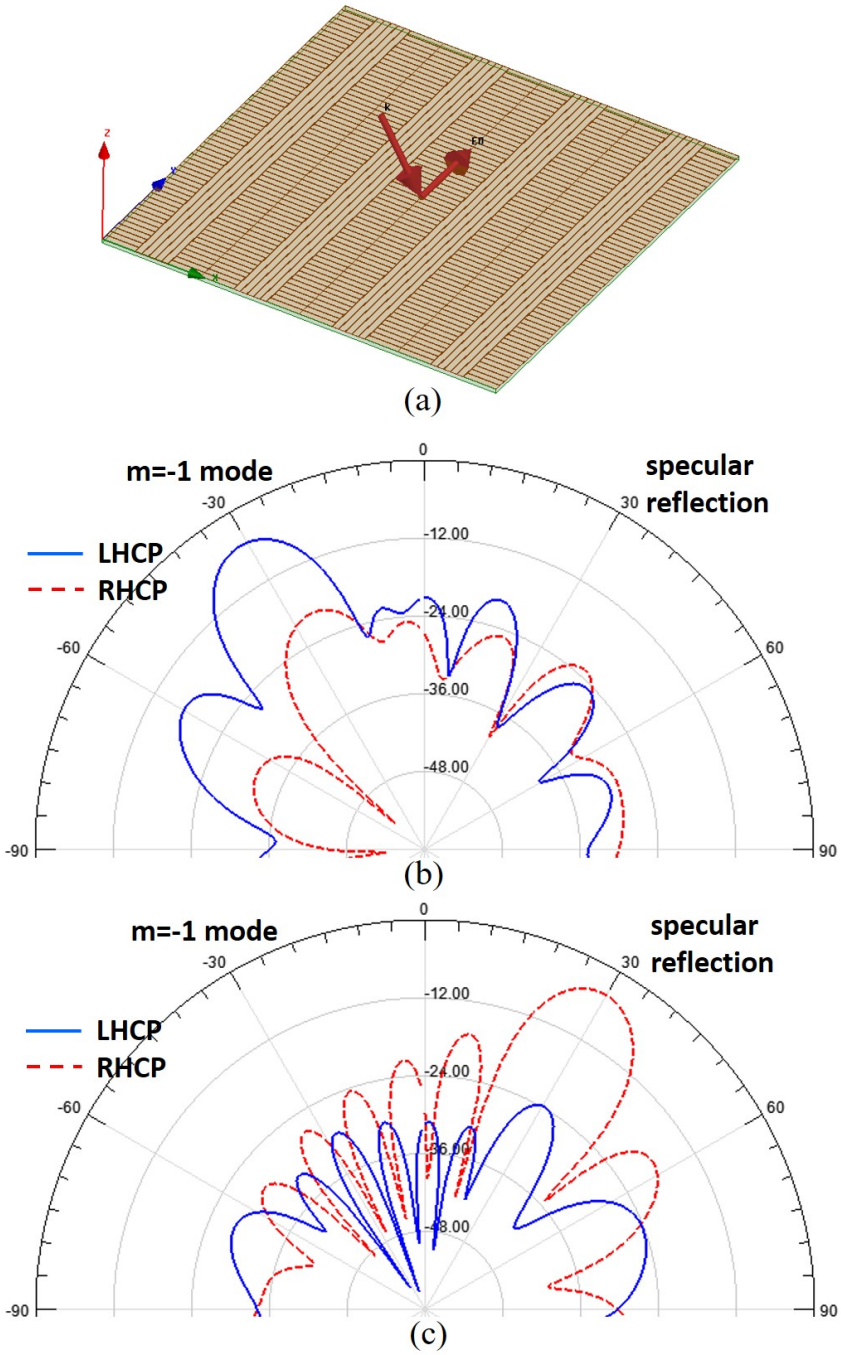

Figure 2.7: Simulated scattering field at 10GHz with LHCP wave incident at $\theta_i = -30^o$(a) A finite 4-cell sample. (b) Simulated scattering (in dB) from metasurface grating. (c) Simulated scattering (in dB) from same size PEC sheet.

phase between TE and TM polarizations in $m = -1$ mode is 151.8^o, which is close to 180^o. Therefore, we can expect a strong $m = -1$ mode with the same handedness as the incident CP wave. It can be noticed that there is a dip in Fig. 2.6a for TM polarization. Such effect is common in blazed gratings for TM polarization, and it has been reported in [41].

To validate the concept, the simulation of the scattering from a finite metasurface grating is performed. The sample is shown in Fig. 2.7a. The size of the structure is 12 cm x 12 cm, i.e. 4 x 4 unit-cells. The incident wave is LHCP at 10 GHz, and the incident angle is $\theta_i = -30^o$. The scattered field of the finite sample is shown in Fig. 2.7b. It can be observed that strong auto-collimation is achieved and there is almost no specular reflection. More importantly, the scattered field in $m = -1$ mode is dominantly LHCP, which is the same handedness as the incident wave. The side lobes are due to the finite size of the scatter, and can be narrower if larger size sample is used.

A similar simulation is made for a 12 cm x 12 cm PEC plate with the same incident wave for comparison. The result is shown in Fig. 2.7c. As we expected, the specular reflection is very strong, and there is no scattered wave in m=-1 mode. Also, the handedness of the specular reflection wave is opposite to the incident wave.

2.4 measurements

2.4.1 Measurement setup

To validate the auto-collimation and handedness preservation effects, experimental sample based on the proposed idea is fabricated and measured (Fig. 2.8). For comparison, a same size sawtooth grating with the blazed angle $\theta_b = 30^o$ is also fabricated and measured (Fig. 2.8).

Fig. 2.9 shows the scheme of the measurement setup. The sample is placed on top of a rotator that can rotate for different incident angles θ_i. An X-band horn antenna is used to illuminate the sample with the linearly polarized (LP) wave. The horn antenna is connected to a vector network analyzer (VNA) to perform one-port measurement. In theory, the

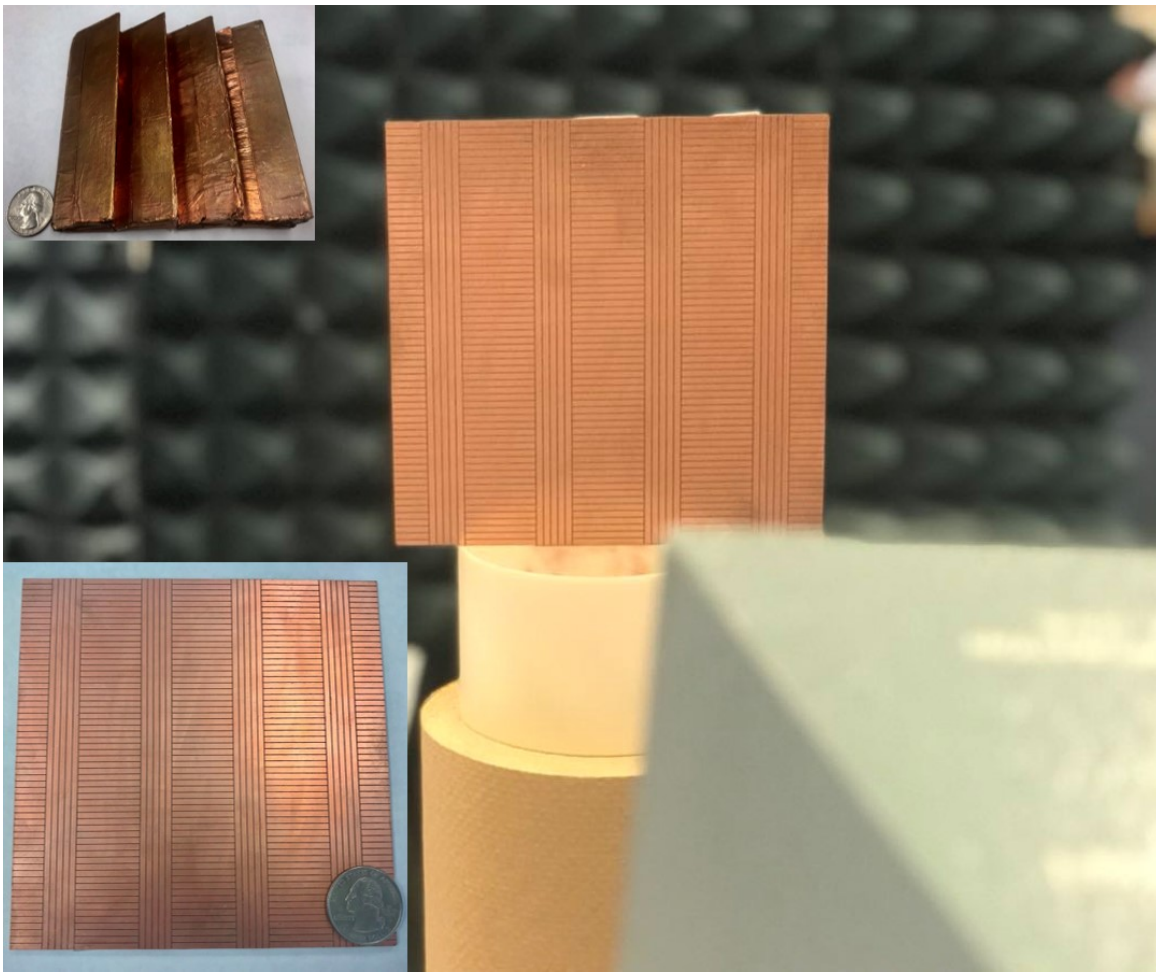

Figure 2.8: Fabricated samples of the metasurface grating and the sawtooth grating, with the picture of the measurement setup.

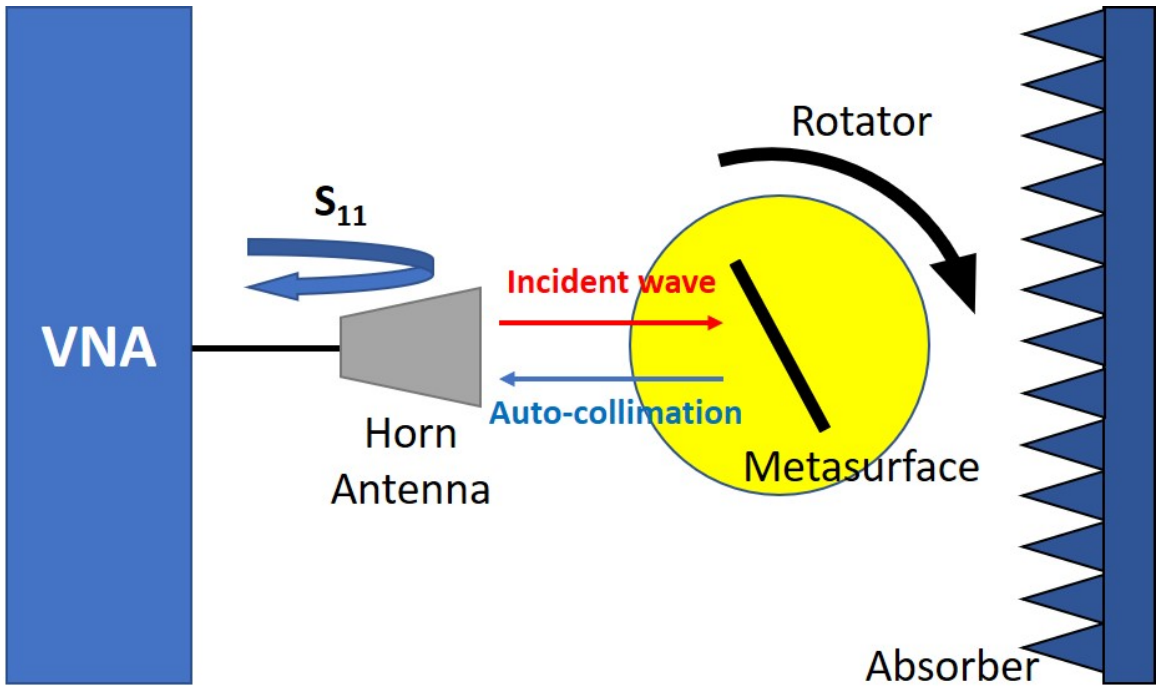

Figure 2.9: Scheme of the measurement setup.

measured S_{11} should correspond to the power that is scattered back from the environment, i.e. the strength of the sample's auto-collimation in this setup. In realty, the port reflection at the horn antenna also contributes to S_{11} and causes interference. Time gating technique is used to eliminate the effect of the port reflection to rule out such interference.

Since the horn antenna can only generate LP wave, the measurements for both horizontal polarization (TM polarization) and vertical polarization (TE polarization) must be performed to evaluate the CP operation of the sample. Denote the measured complex S_{11} for v-pol and h-pol as the magnitude and phase of auto-collimation wave E_h and E_v respectively. In this project, we assume LHCP incident wave. Then the total scattered field in auto-collimation can be written as

$$\vec{E}_{total} = E_h\hat{h} + jE_v\hat{v}, \tag{2.3}$$

where $j = \sqrt{-1}$.

Since LHCP and RHCP are a set of orthogonal basis for plane wave, the total field can

be decomposed as

$$|E_{LHCP}| = |\vec{E}_{total} \cdot \hat{e}_{LHCP}| \tag{2.4a}$$

$$|E_{RHCP}| = |\vec{E}_{total} \cdot \hat{e}_{RHCP}| \tag{2.4b}$$

where

$$\hat{e}_{LHCP} = \frac{1}{\sqrt{2}}(\hat{h} - j\hat{v}) \tag{2.5a}$$

$$\hat{e}_{RHCP} = \frac{1}{\sqrt{2}}(\hat{h} + j\hat{v}). \tag{2.5b}$$

It has to be noted that the definition of LHCP and RHCP in 2.5 seems to be opposite to conventional definition. The reason is that the scattered field in auto-collimation propagates along the opposite direction of the incident wave.

2.4.2 Measurement Result

Fig. 2.10a presents the measurement results of the metasurface grating. The vertical axis represents the synthesized magnitude of the auto-collimation waves. Here, we only presented the result with the strongest blazing appeared in the measurements, which correspond to the incident angle $\theta_i = -28^o$ in this scenario. The red curve is the magnitude of normal reflection from a PEC plate of the same size as the metasurface grating. It serves as the reference. The blue curve represent the LHCP component of the auto-collimation wave, whereas the green dotted curve is the RHCP component. It can be observed that the strongest auto-collimation is achieved at 10.65 GHz, where the magnitude of LHCP is higher than RHCP by 13.39 dB. Meanwhile, the magnitude of the LHCP wave is only 1.13 dB lower than the normal reflection from the PEC plate. This demonstrated a strong auto-collimation so that almost all of the incident LHCP wave is scattered back in LHCP wave in the measurement. The shift of the center frequency is caused by fabrication and measurement errors.

Same measurement is performed on a same size metallic sawtooth grating for comparison. The result is shown in Fig. 2.10b. Again, only the measurement result with the strongest auto-collimation is presented. The incident angle $\theta_i = -31^o$ in this case. The maximum

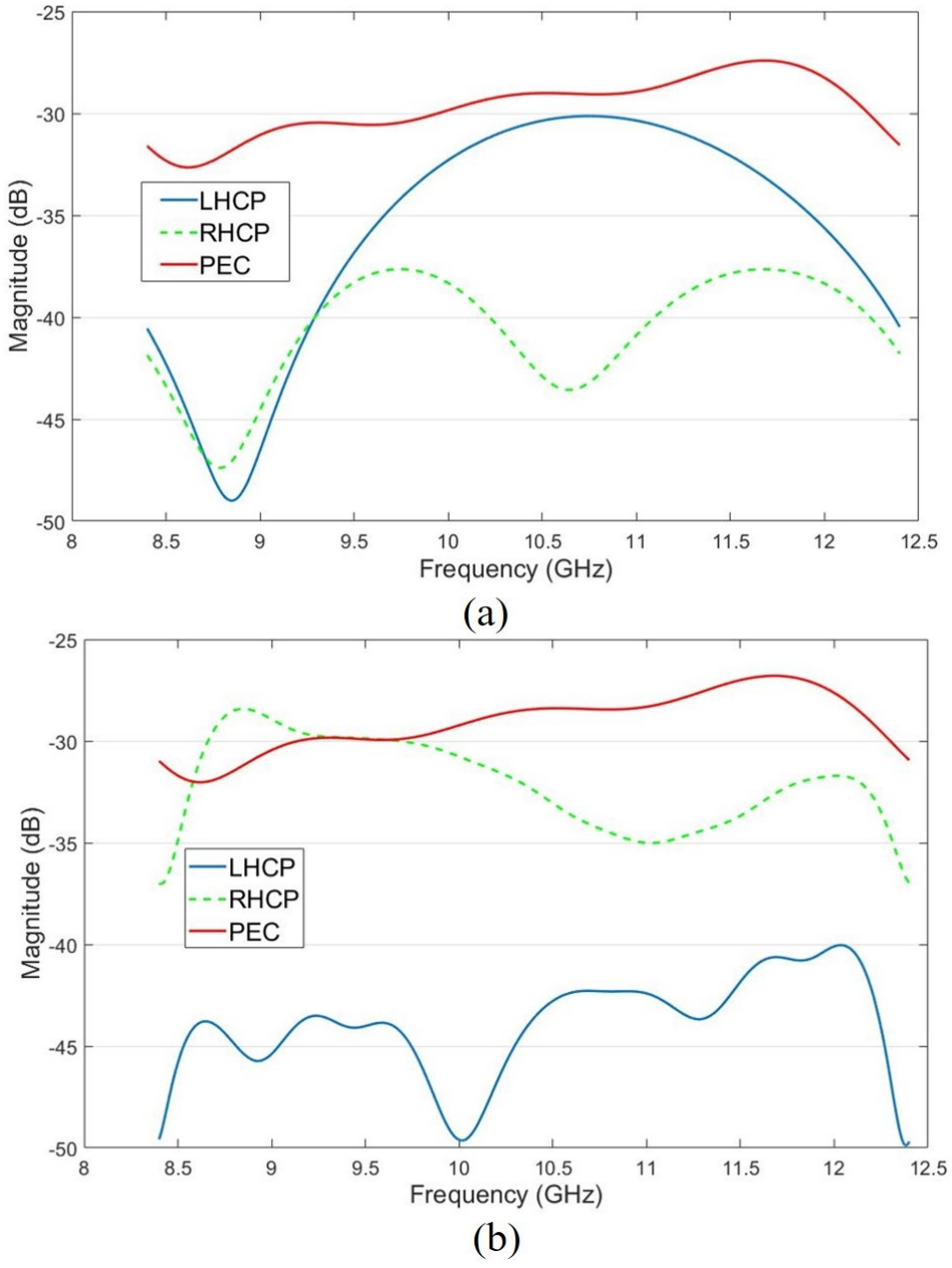

Figure 2.10: Auto-collimation measurements with LHCP incident wave. (a) Proposed metasurface grating. (b) Metallic sawtooth grating.

auto-collimation is achieved at 9.45 GHz and the magnitude of RHCP wave is higher than LHCP wave by 14.2 dB. It can be seen that the most of the incident LHCP wave is scattered into the auto-collimation direction, but the handedness is reversed. In addition, we can see that the auto-collimation wave magnitude of both meatsurface grating and sawtooth grating is around -30dB, which shows that the LHCP handedness preservation is almost as good as a PEC sawtooth reflection of RHCP.

2.5 Conclusion

A novel metasurface grating is proposed and validated to provide both strong auto-collimation and handedness preservation for the CP incident wave. The strong blazing effect is achieved by combining PEC and PMC scatterer according to Bragg condition. Its unique features can be potentially used at microwave, mm-wave, THz, and optical frequencies.

CHAPTER 3

Single-Layer Slow-Wave Substrate Integrated Waveguide with Enhanced Capacitance

3.1 Introduction

The planar transmission line structures, such as microstrip and coplanar waveguide (CPW), have been the fundamental components of RF and microwave engineering [55, 56]. Substrate integrated waveguide (SIW), which was proposed in recent years, has been widely used in high frequencies (typically $>$ 10 GHz) for its high efficiency and compatibility with planar circuits [37, 57–62]. The concept of SIW is quite straight forward. As shown in Fig. 3.1, a rectangular waveguide is formed in a substrate by placing a top metal layer over the ground plane and enclose the structure with rows of though hole vias (THVs) on both sides. However, the applications of SIW at low frequencies are limited because of its high-pass nature. Since it is essentially a rectangular waveguide, the cutoff frequency of SIW is inversely proportional to its broadside dimension. Several studies have been presented to solve this problem, such as substrate integrated folded waveguide (SIFW) [63] and half mode SIW (HMSIW)[64, 65]. Fig. 3.2 shows the geometry of the SIFW and HMSIW. It can be seen that both techniques can reduce the lateral dimension by 50%. Nevertheless, the reduction in longitudinal dimension was not investigated.

To reduce the lateral and longitudinal dimensions of SIW simultaneously, slow-wave effect can be employed. Slowwave structures are waveguides or transmission lines in which the wave travels with a phase velocity equal to or less than a certain predesignated velocity of wave propagation [66].The concept of slow-wave effect has been extensively studied in

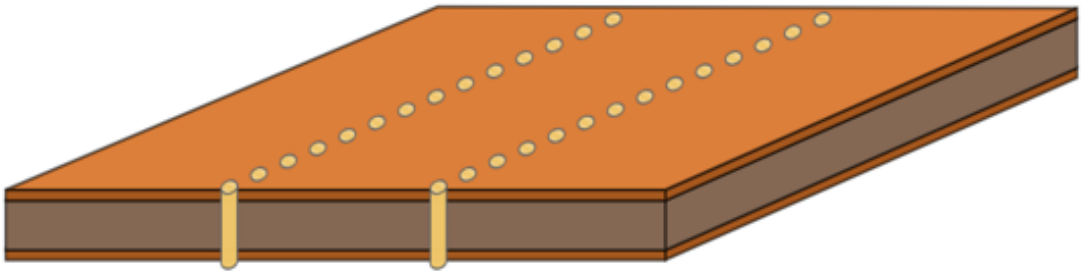

Figure 3.1: Geometry of substrate integrated waveguide.

the conventional transmission line structures to improve the compactness and performances [67–69]. However, it was not until very recently did people start to investigate the slow-wave effect on SIW. To author's best recollection, the first SW-SIW is proposed in [70]. An array of blind vias are loaded into a SIW so that the shunt capacitance is enhanced without significantly disturbing the inductance. As a result, it increases the effective permittivity. However, the blind vias require a multilayer SIW structure. In [71, 72], the SW-SIW are implemented by replacing the top metal layer with a net of microstrip polyline and lumped inductor respectively. The series inductance is enhanced without significantly disturbing the capacitance therefore increases the effective permeability. These structures are presented in Fig. 3.3. These SW-SIW can achieve 40% size reduction in both lateral and longitudinal dimensions.

In this project, a new SW-SIW design based on enhanced capacitance is proposed using single-layer instead of multilayer. The slow-wave effect is achieved by grounded periodic square patches acting as the elevated ground plane. The slow-wave effect provides substantial size reduction in both lateral and longitudinal dimensions. As a demonstration of application, a BPF at 5.6 GHz with a FBW of 7.8% are designed and measured in both conventional and proposed SW-SIW for comparison.

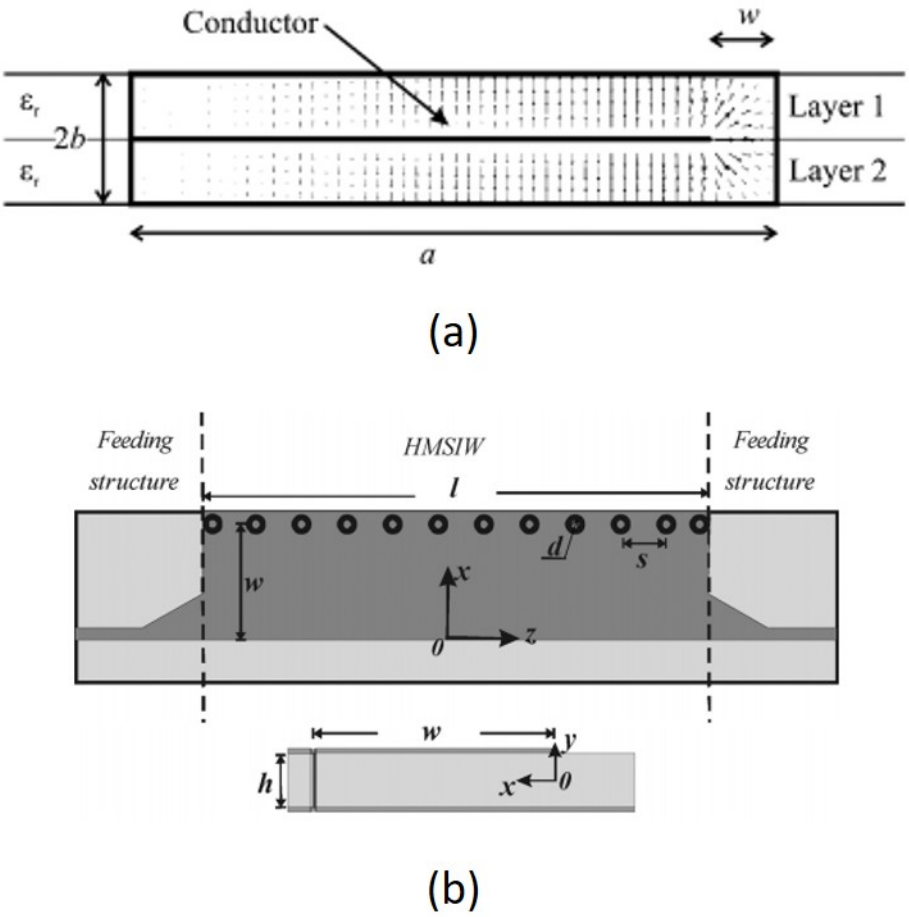

Figure 3.2: (a) Substrate integrated folded waveguides (SIFW). (b) Half-mode substrate integrated waveguide (HMSIW).

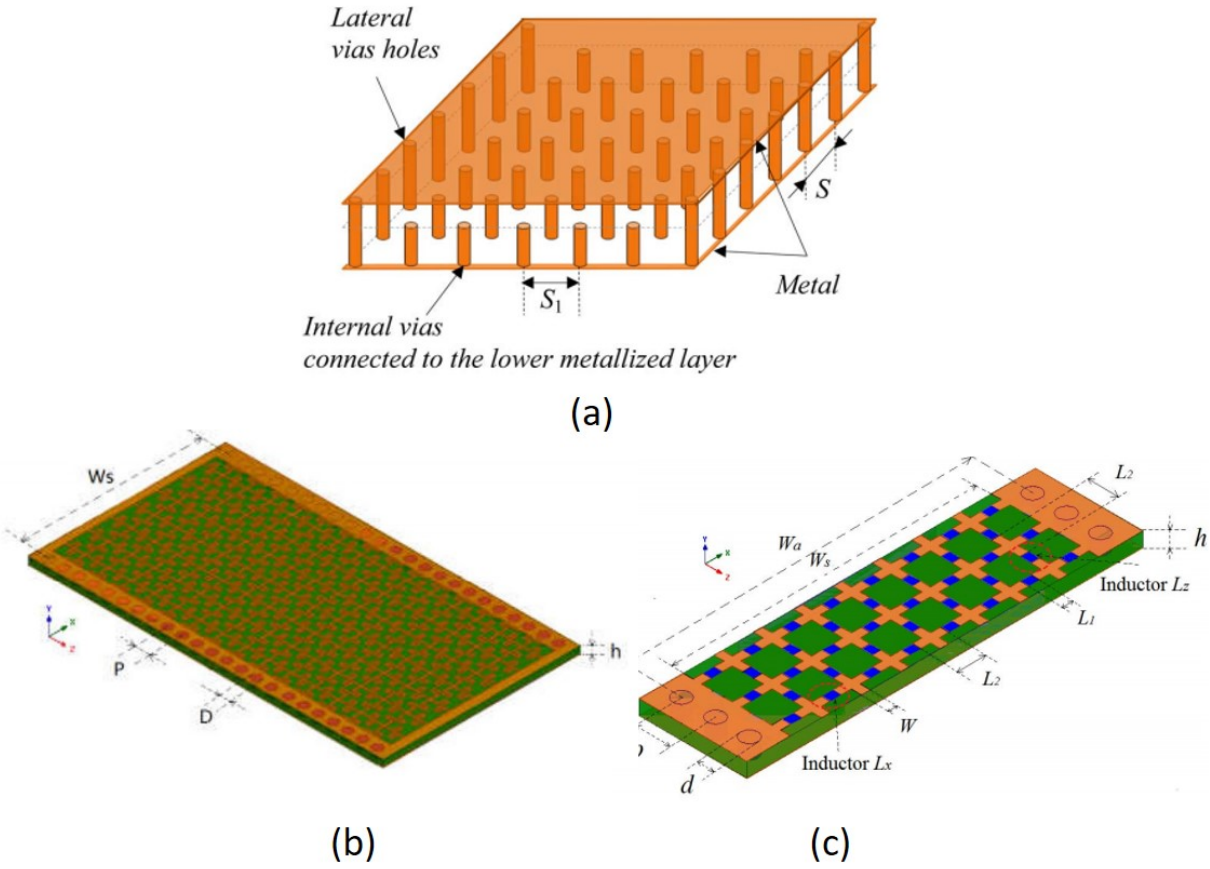

Figure 3.3: SW-SIW implemented with (a) blind vias, (b) microstrip polyline, (c) lump indutors.

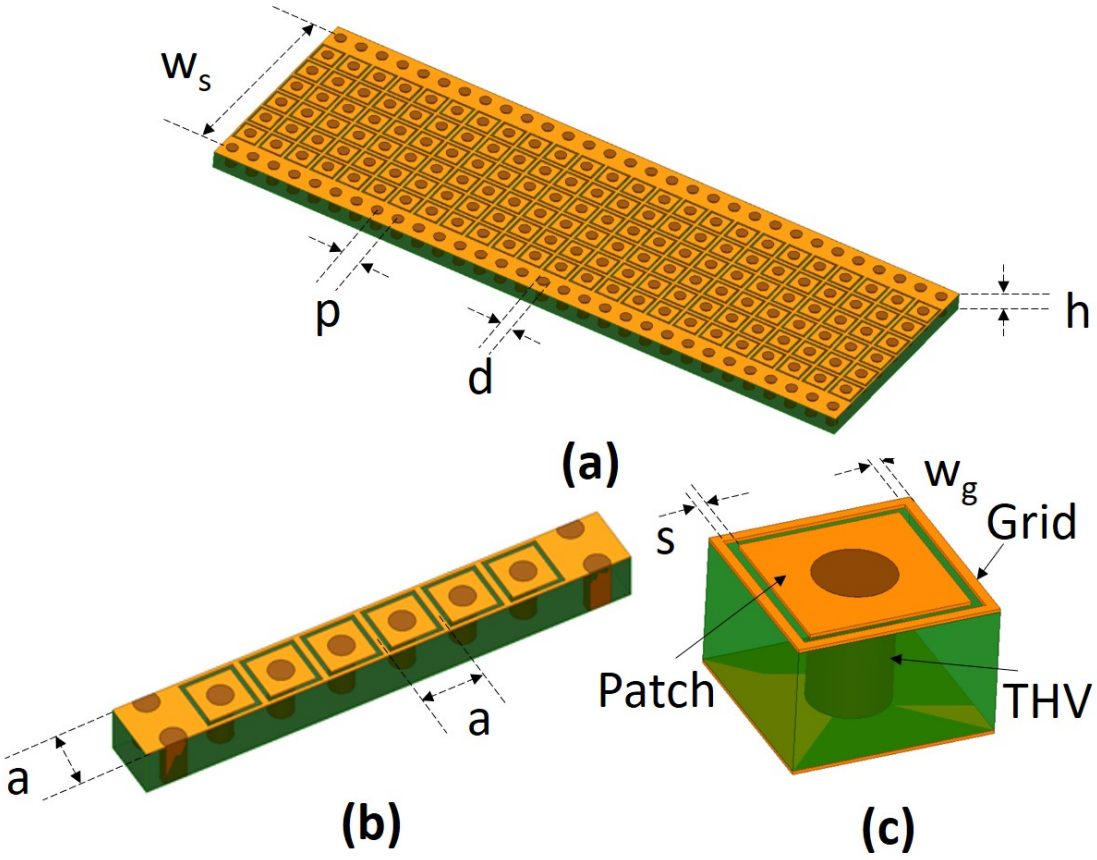

Figure 3.4: Schematic view of proposed SW-SIW : (a) 3-D view. (b) Super-cell of the proposed SW-SIW. (c) Unit cell of the SW-SIW.

3.2 SW-SIW Operation Principle

3.2.1 SW-SIW Topology

Fig. 3.4 presents the topology of the proposed SW-SIW. As shown in Fig. 3.4(a), the proposed circuit is a SIW which consists of periodically cascaded super-cells presented in Fig. 3.4(b). Each of the super-cell is a single-layer structure composed of 6 unit cells shown in Fig. 3.4(c). There is a square patch on the top side in each unit cell, which is connected to the ground by THV. The patch is enclosed by a square slot, whereas the slot is surrounded by a metal grid. The metal grid is corresponding to the top surface of a conventional SIW, and the grounded patches enclosed by the grid are effectively the elevated ground plane.

The slow-wave effect of the proposed structure is investigated with full wave simulations. The substrate is Rogers RO6002 with relative dielectric constant $\epsilon_r = 2.94$, and tangent loss $\tan\delta = 0.0012$. The thickness of the substrate $h = 1.27$ mm and the copper thickness is 35 um. The diameter of THVs for both side wall and unit cell is $d = 0.8$ mm. The length of the unit cell is $a = 2$ mm. The trace width of the grid $w_g = 0.2mm$ and the width of the slot in unit cell is $s = 0.2$ mm.

3.2.2 Electromagnetic Fields

The EM simulation of the proposed SW-SIW is performed form DC to 10 GHz. Fig. 3.5 shows the distribution of electric field and magnetic field in the cross section at 6 GHz. It can be seen that the electric field is concentrated on top surface within the slots. Such concentration indicates a substantial enhancement of the shunt capacitance. On the other hand, the magnetic field exists in the whole volume around the vias and the field distribution is similar to the H-field distribution of TE_{10} mode in a conventional SIW. The separation of E-field and H-field is a typical feature in slow-wave structures.

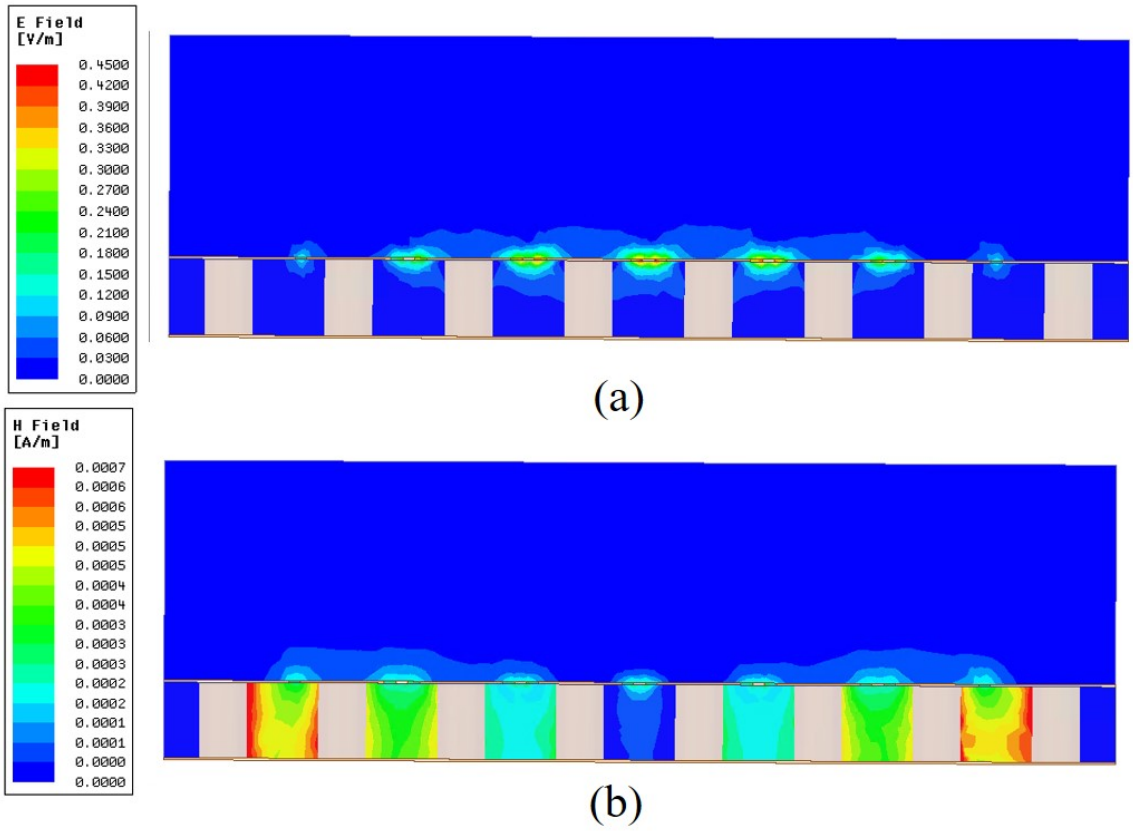

Figure 3.5: Cross section of the proposed SW-SIW : (a) E-field. (b) H-field.

3.2.3 Equivalent Circuit Model

To better understand the properties of the proposed SW-SIW structure, it is important to obtain its equivalent circuit model. The equivalent circuit model in Fig. 3.6b can be extracted intuitively from the side view of the unit-cell shown in Fig. 3.6a. Capacitor C_1, C_3 represent the capacitance between the ground plane, and the grid and patch respectively. Capacitor C_2 represents the enhanced capacitance between the grid and the patch. Inductor $L2$ is the inductance due to the THV, while the series inductor $L1$ is the inductance caused by signal current flowing through the grid.

To verify the equivalent circuit model, a full wave eigenmode simulation is performed on the unit-cell of the proposed SW-SIW, to investigate its dispersion diagram (Fig. 3.7). The x-axis of the figure shows the phase delay when the EM wave travel across the unit-cell, and

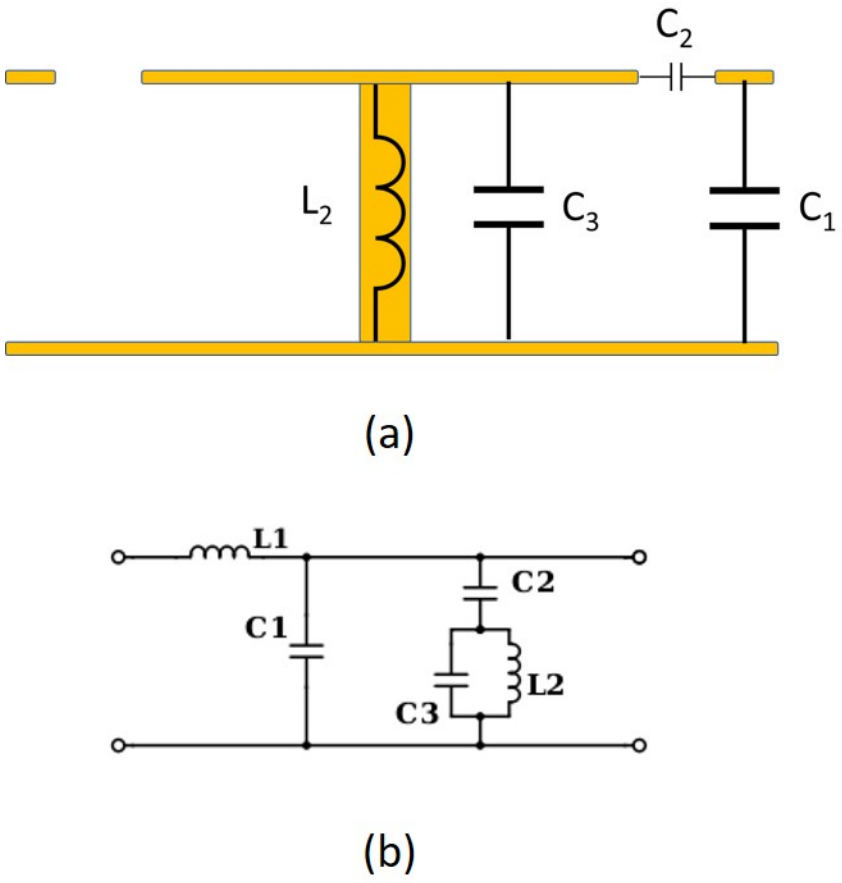

Figure 3.6: (a) Side view of the unit-cell. (b) Equivalent circuit model of the unit-cell.

the y-axis shows the corresponding frequency.

One immediate observation from Fig. 3.7 is that the dispersion curve of the unit-cell is far below the air line, which indicates a strong slow wave effect. On the other hand, it can be seen that the dispersion curve of the unit-cell is quite linear when the phase delay across the unit-cell $\beta d \leq 90°$, i.e. the unit-cell size is smaller than quarter guided wavelength. However, the equivalent circuit model in Fig. 3.6b is not supposed to provide such linear dispersion curve, unless L_2 is close to 0. Nevertheless, from full wave DC simulation, the value of L_2 is not negligible.

The key to the discrepancy between the circuit model and the linearity of the dispersion curve at low frequency is L_2. Since L_2 is induced by the current flow through the THV, full wave simulations are performed to investigate the current on the THV. The simulations are performed at a low frequency (corresponding to $\beta d = 25^o$) and a high frequency (corresponding to $\beta d = 135^o$).

The surface current on the via is presented in Fig. 3.8. At the low frequency, it can be seen that the currents on the two sides of the via are anti-parallel and therefore canceling out. In other words, there is no net current on the via at the low frequency. Hence L_2 effectively does not exist, which explains why the dispersion curve is linear. At the high frequency, however, it can be seen that the currents on the two sides of the via are parallel and therefore adding up. In other words, there is net current, hence L_2 come into the picture. That explains the non-linearity of the dispersion curve at higher frequencies. However, what is the reason behind the different current distributions between low frequencies and high frequencies?

To answer the question, we need to look into the current distribution on the top surface as well. It can be seen from Fig. 3.9a that the current on the grid points towards the same direction along the propagation axis. That is because when the frequency is low, the phase delay across the unit-cell is so small that we can treat it as a DC current. Such treatment is termed as quasi-static approximation and can be employed when the phase delay across the unit-cell $\beta d \leq \pi/2$. To accommodate with the current on the grid, the current on the patch

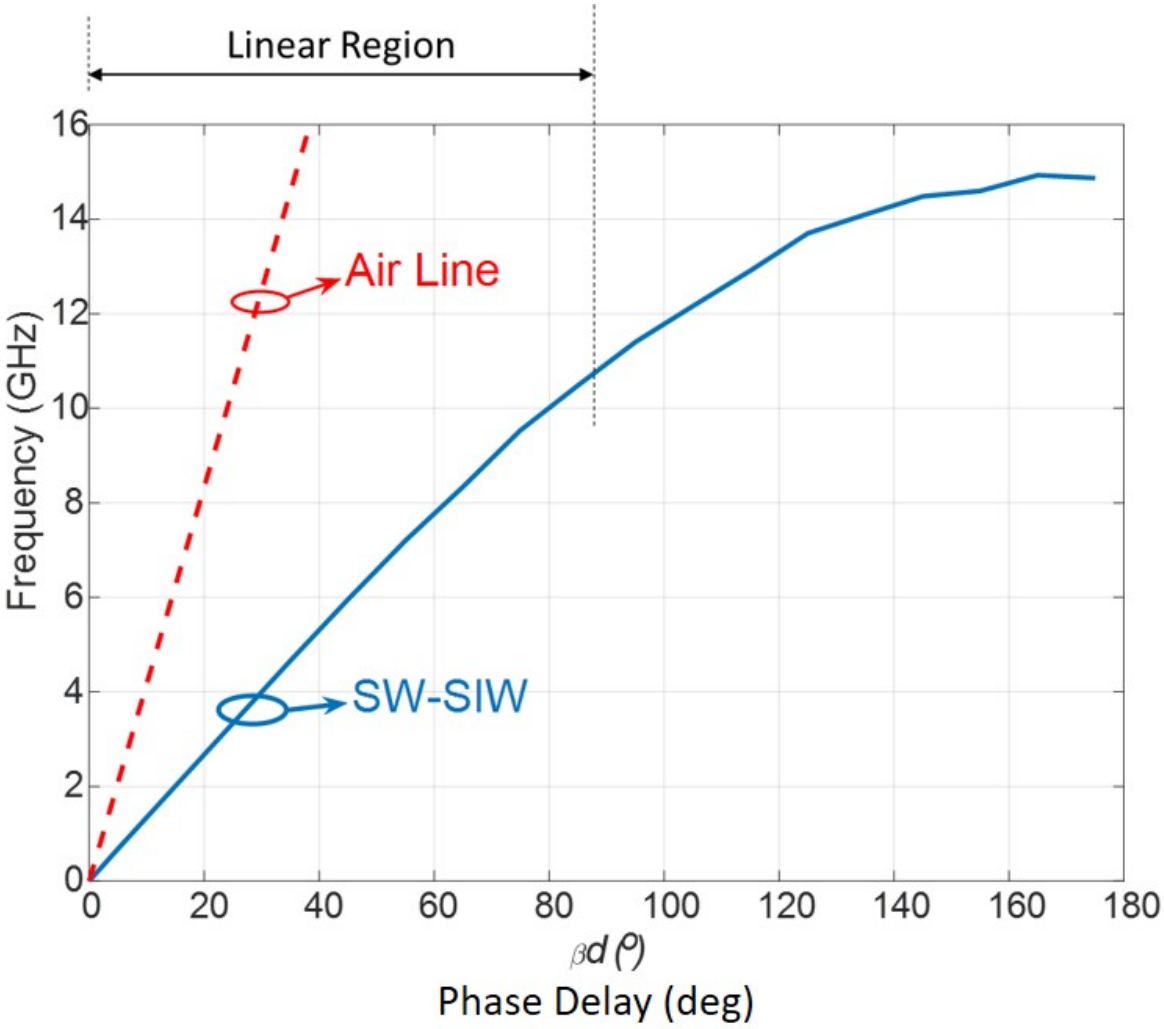

Figure 3.7: Dispersion diagram of the unit-cell of the proposed SW-SIW.

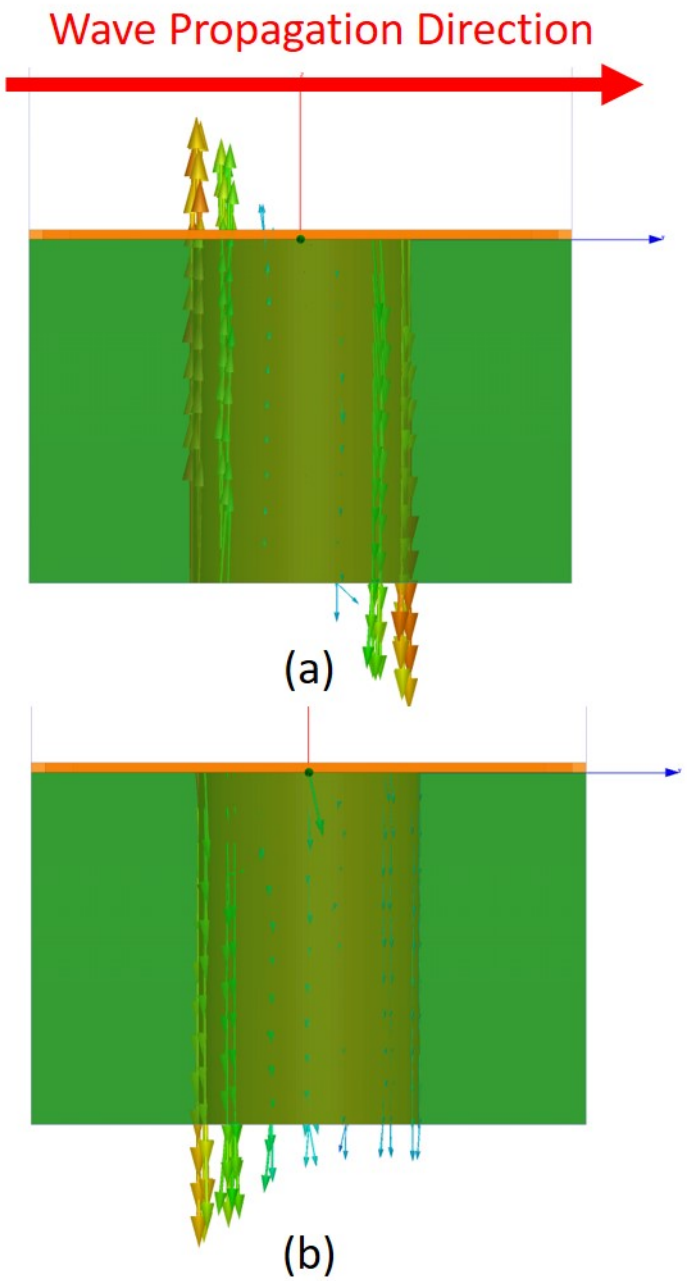

Figure 3.8: Surface current on the THV (a) When phase delay $\beta d = 25°$. (b) When phase delay $\beta d = 135°$.

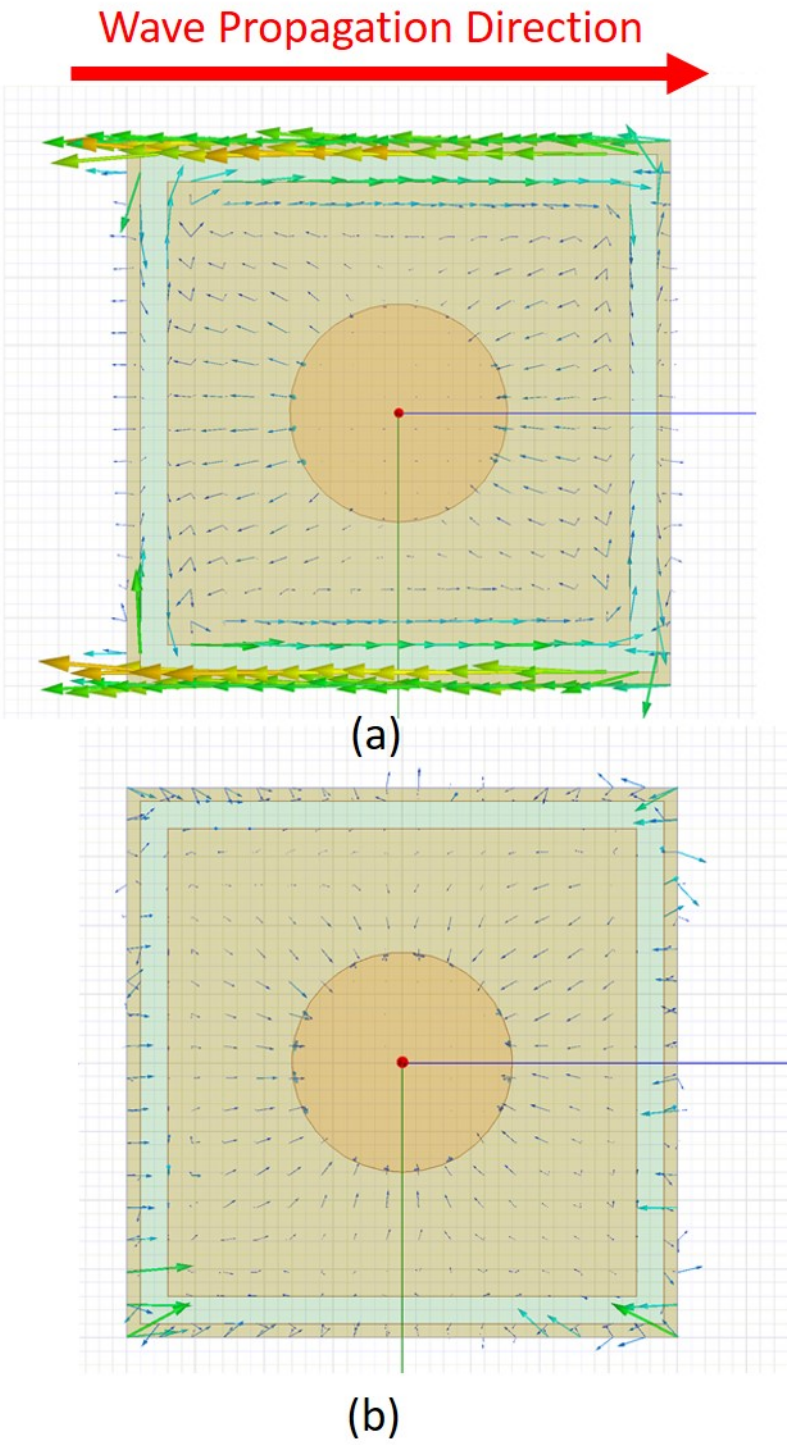

Figure 3.9: Surface current on the top surface (a) When phase delay $\beta d = 25°$. (b) When phase delay $\beta d = 135°$.

forms a loop. The patch current coming out from one side of the via and loop back into the other side of the via, thus causing the canceling currents on the via. On the other hand, at high frequencies, the phase delay across the unit-cell cannot be neglected. It can be seen from Fig. 3.9b that the current on the grid has different orientations along the propagation axis. To accommodate such current on the grid, the current on the patch forms radial path, which will draw or push current through the THV, thus inducting the inductance.

Since we are using the structure as transmission line, the linear region is of interest. From the previous discussion, we know that there is not net current on the via in the linear region. In another word, the top patch has equal potential as the ground plane and therefore is effectively shorted to the ground. Fig. 3.10 shows the equivalent circuit model of the unit-cell in linear region, where $C_{tot} = C_1 + C_2 \parallel C_3$.

3.2.4 Electrical Parameters

In this section, electrical parameters of the proposed SW-SIW are studied by EM simulations to demonstrate the decrease of the normalized cutoff frequency, and the increase in slow wave factor (SWF). Meanwhile, design parameter study is performed. We investigate the impact of s on the slow wave effect, since the enhanced capacitance is mainly dictated by the slot width s,

The normalized cutoff frequency is defined as the ratio between the cutoff frequency of SW-SIW and the cutoff frequency of the SIW with the same width. The normalized cutoff frequencies for different slot width s is shown in Fig. 3.11. It can be seen that as s decreases, the normalized cutoff frequency also decreases because of the increased capacitance between the patch and the grid. When $s = 0.1$ mm, the normalized cutoff frequency is 0.577, which implies a 42.3% lateral dimension reduction with a given cut off frequency.

The SWF versus frequency for different slot width s is shown in Fig. 3.12. Here, the SWF is defined by $\frac{c_0}{v_p}$, where v_p and c_o are phase velocity of the guided wave and the speed of light in free space respectively. It can be observed that the SWF increases as s decreases. It is because of the enhanced capacitance as previously discussed. For comparison, the

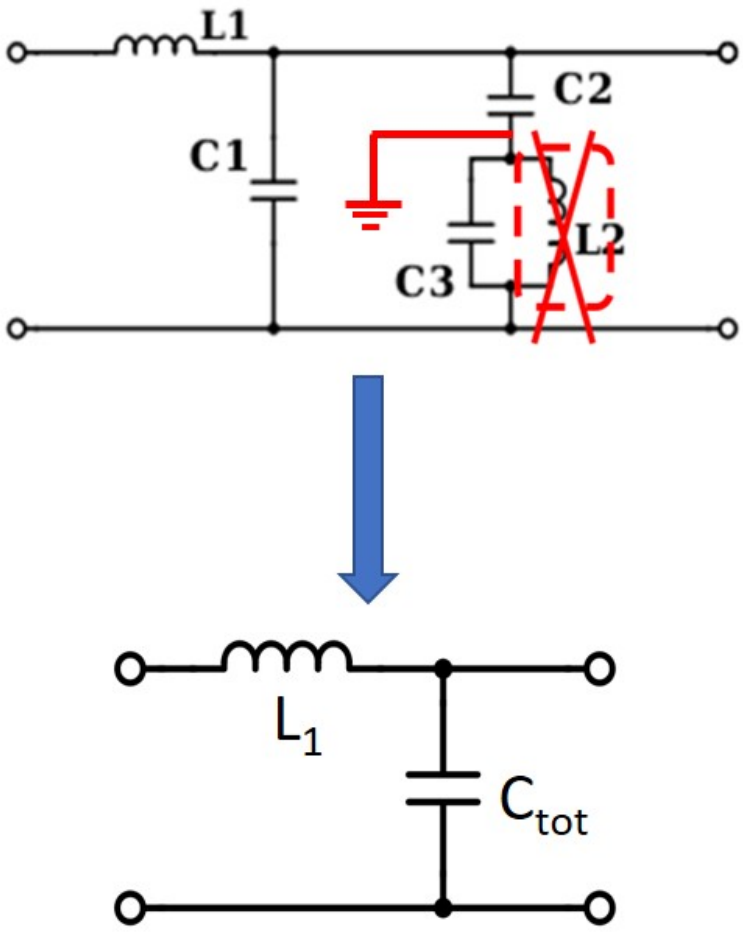

Figure 3.10: The equivalent circuit model of the unit-cell in linear region.

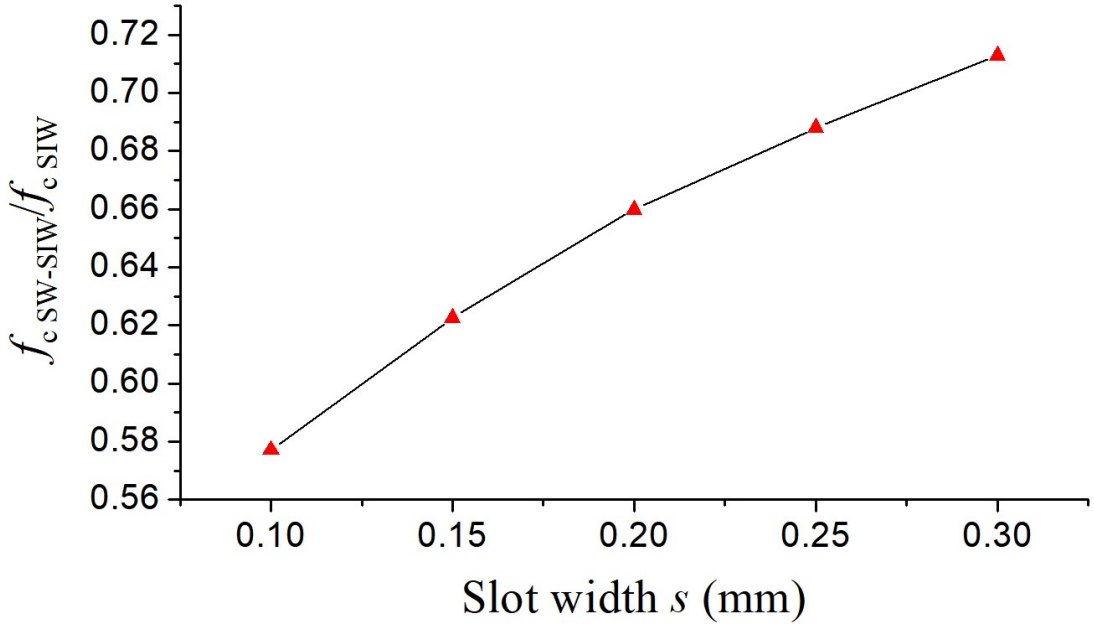

Figure 3.11: Normalized cutoff frequency for different slot width s

SWF of SIW with the same literal dimension is also shown in the figure. Apparently the proposed SW-SIW generally has much larger SWF compared with conventional SIW. Hence, a significant size reduction in longitudinal dimensions can be obtained for a given electrical length.

To be used as transmission line, the efficiency of the proposed SW-SIW is crucial. Hence the attenuation versus frequency is studied for both $s = 0.15$ mm and $s = 0.3$ mm (Fig. 3.13). It can be seen that the attenuation for the SW-SIW is generally less than 0.01 dB/mm, which is similar compared with the aforementioned SW-SIW structures in [70–72]. Such attenuation level is satisfactory, especially when compared with some flexible circuit technology [73–78]. When slot width s is smaller, the attenuation is larger due to the higher E-field concentration in the slot. The dielectric loss is increased in this scenario. Thus a trade off between efficiency and slow-wave effect has to be made when designing such structure.

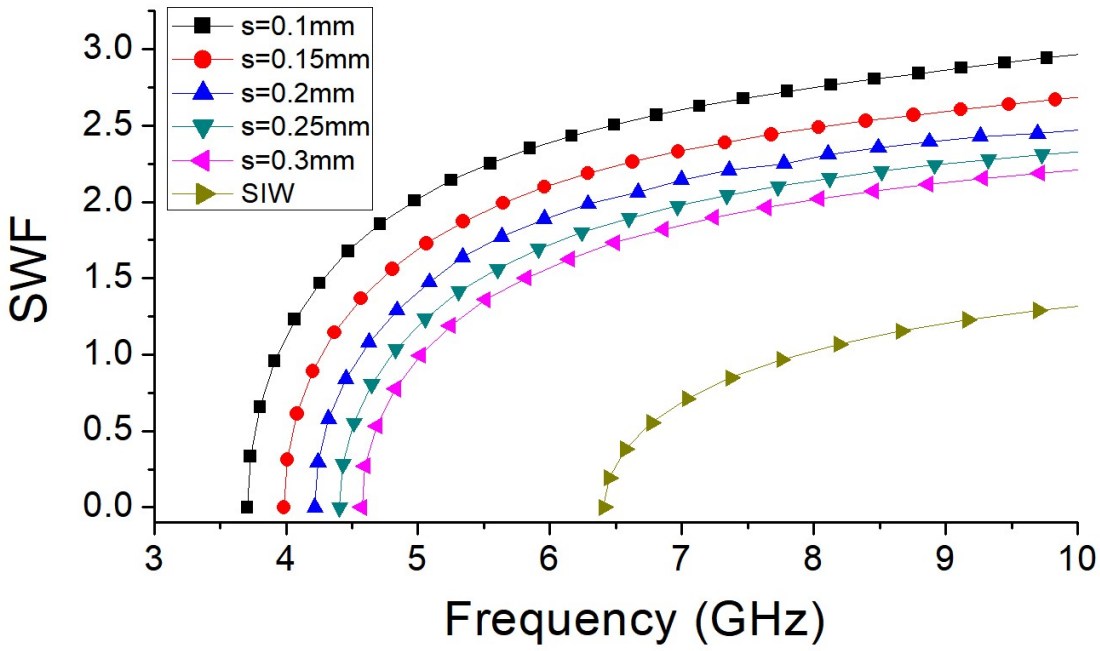

Figure 3.12: SWF versus frequency for different slot width s

3.3 Demonstration of Applications

To demonstrate the application of the proposed SW-SIW, two BPF are designed and measured using both conventional SIW and the new SW-SIW. Both BPF have a center frequency at 5.6 GHz and a FBW 7.8%. The same substrate is used and the slot width is chosen to be $s = 0.2$ mm.

As shown in Fig.3.14a, the filter with SW-SIW consists of 2 cavities. Each cavity has 7 by 5 unit-cells. The two cavities are then cascaded together through a window for controlling coupling by removing certain number of the vias in between. An additional unit-cell is put within the window as a supplementary bridge. For impedance matching, a special matching line is designed. It is a conventional 50Ω microstrip loaded with 1 column of the unit cell in Fig.3.4(c). The microstrip line width is 3.2 mm, and the slot width s for unit cell in feed line is 0.3 mm. Loading similar unit-cell into feeding microstrip line as transition was used in [70] as well. The dimension of SW-SIW BPF is 16 mm × 24 mm.

The SIW BPF follows the same principle. Each of the resonator has a similar width to

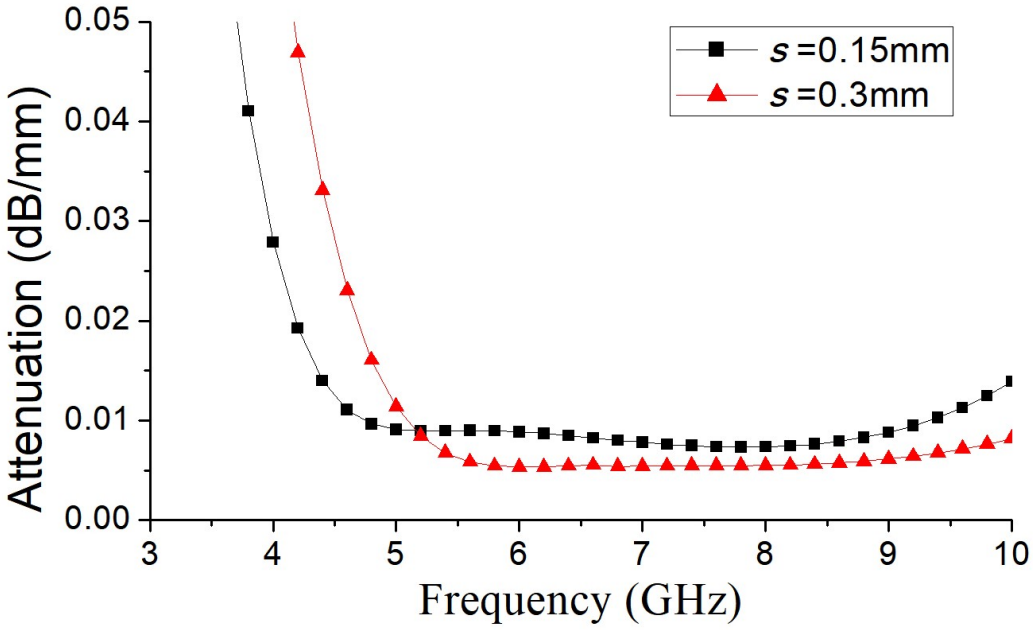

Figure 3.13: Attenuation versus frequency for different slot width s

length ratio with its slow-wave counterpart (Fig. 3.14(b)). For convenience of fabrication, a larger via with a diameter of 1.6 mm is used in this case. The dimension for this filter is 24.2mm × 38.5 mm.

Table 3.1: Simulated and Measured IL, FBW, and Q_u

	SIW BPF	SW-SIW BPF
Sim. FBW	7.8%	7.8%
Mea. FBW	7.8%	8.2%
Sim. IL (dB)	0.50	0.92
Mea. IL (dB)	0.88	1.97
Sim. Q_u	458.4	255.1
Mea. Q_u	266.1	120.2

The simulation and measurement S-Parameter for both filters are shown in Fig. 3.15. The simulated and measured IL, FBW, and Q_u are summarized in table 3.1. The response for both BPFs are very similar according to Fig.3.15. From table 3.1, the measured IL of SW-SIW BPF is 1.05 dB higher than simulated results. The additional losses may result

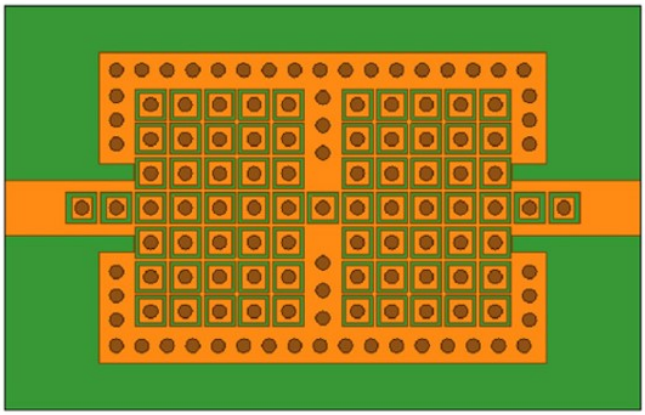

(a)

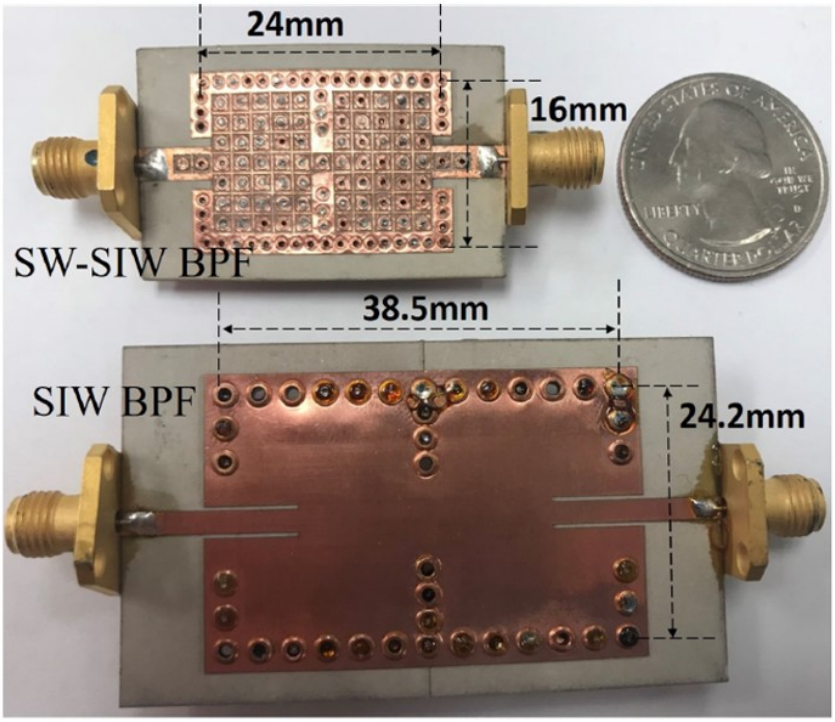

(b)

Figure 3.14: Fabricated bandpass filter using conventional SIW and proposed SW-SIW

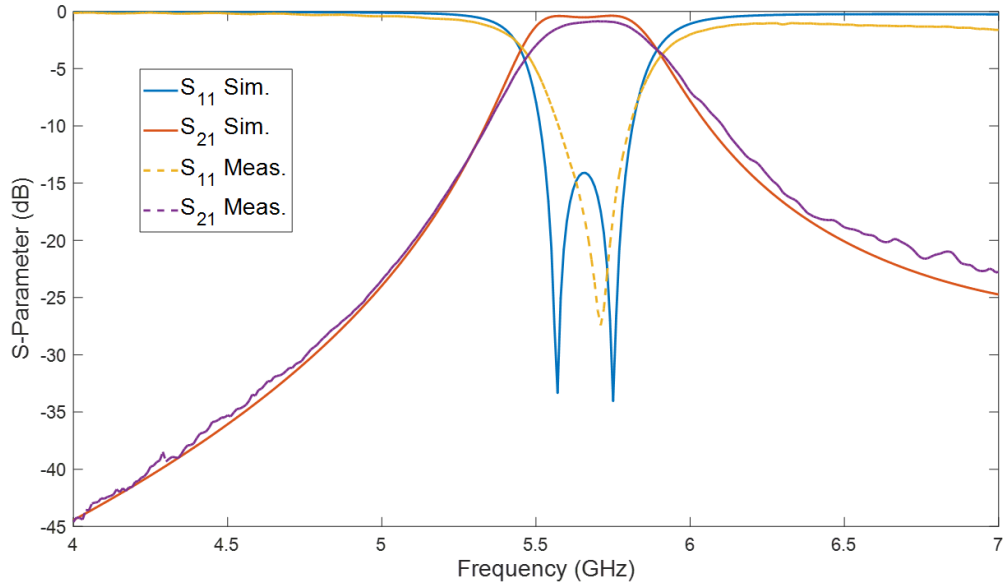

(a)

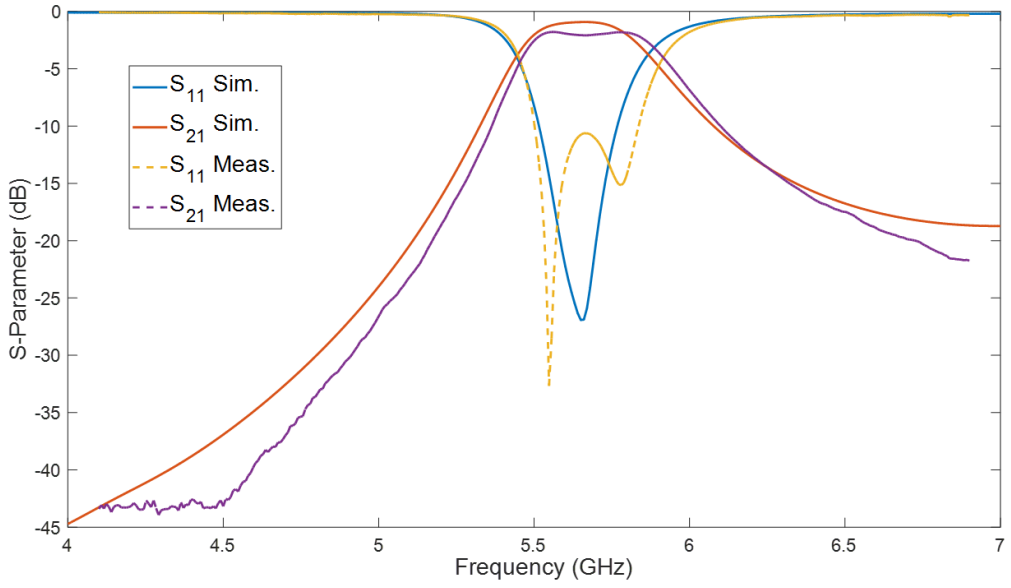

(b)

Figure 3.15: Simulation and measurement results for bandpass filters. (a) Conventional SIW bandpass filter. (b) SW-SIW bandpass filter.

from fabrication errors.

Compared with the conventional SIW BPF, BPF using the proposed SW-SIW achieves 58.8 % of size reduction with reasonable performance. The size reduction can get further improvement by using a smaller slot width s. It also has to be noted that the measured unloaded quality factor $Q_u = 120.2$ for our SW-SIW, which is way higher than typical HMSIW technique. HMSIW is the most commonly used technique for SIW resonator size reduction. Due to its radiation loss at the open edge, the unloaded quality Qu is typically less than 100. Therefore, the proposed SW-SIW achieves both greater size reduction and efficiency compared with HMSIW.

3.4 Conclusion

A novel single layer SW-SIW is proposed and demonstrated more than 40% size reduction in both lateral and longitudinal dimensions. The two effects together lead to a greater size reduction. The equivalent circuit model for the unit-cell is given and justified. Several electrical parameters, such as normalized cutoff frequency, SWF, attenuation is investigated through parametric sweep on the slot width s. As a demonstration, two BPFs are designed and measured using the proposed SW-SIW and SIW. With a reasonable performance, SW-SIW BPF achieves a 58.8% size reduction and an unloaded quality factor of 120.2. This technology has potential applications in microwave, millimeter wave, and CMOS based circuits.

BIBLIOGRAPHY

[1] Robert E Collin. *Field theory of guided waves.* McGraw-Hill, New York, NY, USA, 1960.

[2] Roger F. Harrington. *Time-harmonic electromagnetic fields.* McGraw-Hill, New York, NY, USA, 1961.

[3] Constantine A Balanis. *Advanced engineering electromagnetics.* John Wiley & Sons, Hoboken, NJ, USA, 2 edition, 2012.

[4] David M Pozar. *Microwave engineering.* John Wiley & Sons, Hoboken, NJ, USA, 4 edition, 2011.

[5] Eric Plum and Nikolay I Zheludev. Chiral mirrors. *Appl. Physics Lett.*, 106(22):221901, 2015.

[6] Xu Fang, Kevin F MacDonald, Eric Plum, and Nikolay I Zheludev. Coherent control of light-matter interactions in polarization standing waves. *Scientific Rep.*, 6, August 2016.

[7] Christophe Caloz and Tatsuo Itoh. *Electromagnetic metamaterials: transmission line theory and microwave applications.* John Wiley & Sons, 2005.

[8] Christophe Caloz, Tatsuo Itoh, and Andre Rennings. Crlh metamaterial leaky-wave and resonant antennas. *IEEE Antennas Propag. Mag.*, 50(5), November 2008.

[9] Xiaoqiang Li, Mohammad Memarian, and Tatsuo Itoh. A new cavity resonance assisted by anisotropic metasurfaces. *IEEE Transactions on Microwave Theory and Techniques*, 2018.

[10] Xiaqiang Li, Mohammad Memarian, and Tatsuo Itoh. A new resonance in a circular waveguide cavity assisted by anisotropic metasurfaces. In *IEEE MTT-S Int. Microw. Symp.*, Honululu, HI, USA, Jun. 4-9 2017.

[11] Christopher L Holloway, DC Love, EF Kuester, Alesandro Salandrino, and Nader Engheta. Sub-wavelength resonators: on the use of metafilms to overcome the $\lambda/2$ size limit. *IET Microw., Antennas & Propag.*, 2(2):120–129, March 2008.

[12] Christopher L Holloway, Edward F Kuester, and David Novotny. Waveguides composed of metafilms/metasurfaces: the two-dimensional equivalent of metamaterials. *IEEE Antennas Wireless Propag. Lett.*, 8:525–529, March 2009.

[13] Nader Engheta and Philippe Pelet. Mode orthogonality in chirowaveguides. *IEEE Trans. Microw. Theory Tech.*, 38(11):1631–1634, November 1990.

[14] Fei-Ran Yang, Kuang-Ping Ma, Yongxi Qian, and Tatsuo Itoh. A novel tem waveguide using uniplanar compact photonic-bandgap (UC-PBG) structure. *IEEE Trans. Microw. Theory Tech.*, 47(11):2092–2098, November 1999.

[15] Dan Sievenpiper, Lijun Zhang, Romulo FJ Broas, Nicholas G Alexopolous, and Eli Yablonovitch. High-impedance electromagnetic surfaces with a forbidden frequency band. *IEEE Trans. Microw. Theory Tech.*, 47(11):2059–2074, November 1999.

[16] Alexandros P Feresidis, George Goussetis, Shenhong Wang, and John C Vardaxoglou. Artificial magnetic conductor surfaces and their application to low-profile high-gain planar antennas. *IEEE Trans. Antennas Propag.*, 53(1):209–215, January 2005.

[17] Douglas J Kern, Douglas H Werner, Agostino Monorchio, Luigi Lanuzza, and Michael J Wilhelm. the design synthesis of multiband artificial magnetic conductors using high impedance frequency selective surfaces. *IEEE Trans. Antennas Propag.*, 53(1):8–17, January 2005.

[18] Habib Rostami, Yaser Abdi, and Ezatollah Arzi. Fabrication of optical magnetic mirrors using bent and mushroom-like carbon nanotubes. *Carbon*, 48(13):3659–3666, November 2010.

[19] Sheng Liu et al. Optical magnetic mirrors without metals. *Optica*, 1(4):250–256, October 2014.

[20] RE Collin. A simple artificial anisotropic dielectric medium. *IRE Trans. on Microw. Theory and Techn.*, 6(2):206–209, April 1958.

[21] Gabriele Minatti, Stefano Maci, Paolo De Vita, Angelo Freni, and Marco Sabbadini. A circularly-polarized isoflux antenna based on anisotropic metasurface. *IEEE Trans. Antennas Propag.*, 60(11):4998–5009, November 2012.

[22] Francesco Aieta, Patrice Genevet, Nanfang Yu, Mikhail A Kats, Zeno Gaburro, and Federico Capasso. Out-of-plane reflection and refraction of light by anisotropic optical antenna metasurfaces with phase discontinuities. *Nano Lett.*, 12(3):1702–1706, February 2012.

[23] Y Zhao, MA Belkin, and A Alù. Twisted optical metamaterials for planarized ultrathin broadband circular polarizers. *Nature Commun.*, 3:870, May 2012.

[24] Menglin LN Chen, Li Jun Jiang, and Wei EI Sha. Artificial perfect electric conductor-perfect magnetic conductor anisotropic metasurface for generating orbital angular momentum of microwave with nearly perfect conversion efficiency. *J. of Appl. Physics*, 119 (6):064506, February 2016.

[25] Xiaqiang Li, Mohammad Memarian, Kirti Dhwaj, and Tatsuo Itoh. Blazed metasurface grating: The planar equivalent of a sawtooth grating. In *IEEE MTT-S Int. Microw. Symp.*, San Francisco, CA, USA, May. 22-27 2016.

[26] P-S Kildal. Artificially soft and hard surfaces in electromagnetics. *IEEE Trans. Antennas Propag.*, 38(10):1537–1544, October 1990.

[27] Hossein Mosallaei and Kamal Sarabandi. Antenna miniaturization and bandwidth enhancement using a reactive impedance substrate. *IEEE Trans. Antennas Propag.*, 52 (9):2403–2414, September 2004.

[28] Liwei Lin, Roger T Howe, and Albert P Pisano. Microelectromechanical filters for signal processing. *J. of Microelectromechanical Syst.*, 7(3):286–294, 1998.

[29] Kun Wang and CT-C Nguyen. High-order medium frequency micromechanical electronic filters. *J. of Microelectromechanical Syst.*, 8(4):534–556, December 1999.

[30] Winter Dong Yan and Raafat R Mansour. Tunable dielectric resonator bandpass filter with embedded mems tuning elements. *IEEE Trans. Microw. Theory Tech.*, 55(1): 154–160, January 2007.

[31] Matjaz Humar, Miha Ravnik, Stane Pajk, and Igor Muševič. Electrically tunable liquid crystal optical microresonators. *Nature Photonics*, 3(10):595–600, September 2009.

[32] Raafat R Mansour. High-q tunable dielectric resonator filters. *IEEE Microw. Mag.*, 10 (6), September 2009.

[33] Xiaoguang Liu, Linda PB Katehi, William J Chappell, and Dimitrios Peroulis. High-q tunable microwave cavity resonators and filters using soi-based rf mems tuners. *J. of Microelectromechanical Syst.*, 19(4):774–784, August 2010.

[34] Stephen M Hou, Jeffrey H Lang, Alexander H Slocum, Alexis C Weber, and James R White. A high-q widely tunable gigahertz electromagnetic cavity resonator. *J. of Microelectromechanical Syst.*, 15(6):1540–1545, December 2006.

[35] Ryan C Gough, Jonathan H Dang, Matthew R Moorefield, George B Zhang, Lloyd H Hihara, Wayne A Shiroma, and Aaron T Ohta. Self-actuation of liquid metal via redox reaction. *ACS Appl. Materials & Interfaces*, 8(1):6–10, 2015.

[36] Mohammad Memarian and Raafat R Mansour. Quad-mode and dual-mode dielectric resonator filters. *IEEE Trans. Microw. Theory Tech.*, 57(12):3418–3426, December 2009.

[37] Kirti Dhwaj, Xiaoqiang Li, Zhi Shen, and Shihan Qin. Cavity resonators do the trick: A packaged substrate integrated waveguide, dual-band filter. *IEEE Microwave Magazine*, 17(1):58–64, 2016.

[38] Tatsuo Itoh and R Mittra. An analytical study of the echelette grating with application

to open resonators. *IEEE Transactions on Microwave Theory and Techniques*, 17(6): 319–327, 1969.

[39] A Hessel, J Schmoys, and DY Tseng. Bragg-angle blazing of diffraction gratings. *JOSA*, 65(4):380–384, 1975.

[40] EV Jull, JW Heath, and GR Ebbeson. Gratings that diffract all incident energy. *JOSA*, 67(4):557–559, 1977.

[41] EG Loewen, Maystre Nevière, and D Maystre. Grating efficiency theory as it applies to blazed and holographic gratings. *Applied optics*, 16(10):2711–2721, 1977.

[42] KA Jose and KG Nair. Reflector-backed perfectly blazed strip gratings simulate corrugated reflector effects. *Electronics Letters*, 23(2):86–87, 1987.

[43] Nanfang Yu and Federico Capasso. Flat optics with designer metasurfaces. *Nature materials*, 13(2):139, 2014.

[44] CJ Hawthorn, KP Weber, and RE Scholten. Littrow configuration tunable external cavity diode laser with fixed direction output beam. *Review of scientific instruments*, 72(12):4477–4479, 2001.

[45] Xiaoqiang Li. Circularly polarized low side lobe level composite right/left-handed siw leaky wave antenna and blazed metasurface, 2016.

[46] Jordan Budhu and Yahya Rahmat-Samii. An efficient spectral domain method of moments for reflectarray antennas using a customized impedance matrix interpolation scheme. In *Radio Science Meeting (USNC-URSI NRSM), 2013 US National Committee of URSI National*, pages 1–1. IEEE, 2013.

[47] Jordan Budhu and Yahya Rahmat-Samii. Accelerating the spectral domain moment method for reflectarray's by two-orders of magnitude. In *Antennas and Propagation Society International Symposium (APSURSI), 2013 IEEE*, pages 1340–1341. IEEE, 2013.

[48] Mohammad Memarian, Xiaoqiang Li, and Tatsuo Itoh. Resonant blazed metasurface gratings. In *Microwave Conference (EuMC), 2016 46th European*, pages 297–300. IEEE, 2016.

[49] Mohammad Memarian, Xiaoqiang Li, Yasuo Morimoto, and Tatsuo Itoh. Wide-band/angle blazed surfaces using multiple coupled blazing resonances. *Scientific Reports*, 7:42286, 2017.

[50] Haozhan Tian, Mohammad Memarian, and Tatsuo Itoh. Electronically-tunable resonant blazed metasurface grating. In *Microwave Conference (APMC), 2017 IEEE Asia Pacific*, pages 376–379. IEEE, 2017.

[51] Haozhan Tian and Tatsuo Itoh. All-polarization blazed surface. In *Microwave Conference (APMC), 2018 IEEE Asia Pacific*. IEEE, 2018.

[52] Cheng Tao, Mohammad Memarian, Yasuo Morimoto, and Tatsuo Itoh. Non-periodic metasurfaces for blazing and beam splitting. In *Microwave Conference (APMC), 2016 Asia-Pacific*, pages 1–4. IEEE, 2016.

[53] Cheng Tao, Xiaoqiang Li, and Tatsuo Itoh. Two-dimensional non-periodic metasurface for dual polarization retroreflection. In *Microwave Conference (EuMC), 2018 48th European*, pages 1194–1197. IEEE, 2018.

[54] Xiaoqiang Li, Cheng Tao, Jiang Lijun, and Tatsuo Itoh. Blazed metasurface grating with handedness preservation for circularly polarized incident wave. In *Microwave Conference (EuMC), 2018 48th European*, pages 133–136. IEEE, 2018.

[55] Thomas G Bryant and Jerald A Weiss. Parameters of microstrip transmission lines and of coupled pairs of microstrip lines. *IEEE Transactions on Microwave Theory and Techniques*, 16(12):1021–1027, 1968.

[56] Cheng P Wen. Coplanar waveguide: A surface strip transmission line suitable for nonreciprocal gyromagnetic device applications. *IEEE Transactions on Microwave Theory and Techniques*, 17(12):1087–1090, 1969.

[57] Dominic Deslandes and Ke Wu. Integrated microstrip and rectangular waveguide in planar form. *IEEE Microwave and Wireless Components Letters*, 11(2):68–70, 2001.

[58] Kirti Dhwaj, Xiaoqiang Li, Lijun Jiang, and Tatsuo Itoh. Low profile diplexing filter/antenna based on common radiating cavity with quasi-elliptic response. *IEEE Antennas and Wireless Propagation Letters*, 2018.

[59] Kirti Dhwaj, Joshua M Kovitz, Haozhan Tian, Li Jun Jiang, and Tatsuo Itoh. Half-mode cavity-based planar filtering antenna with controllable transmission zeroes. *IEEE Antennas and Wireless Propagation Letters*, 17(5):833–836, 2018.

[60] Kirti Dhwaj, Yan Zhao, Richard Al Hadi, Xiaoqiang Li, Frank M-C Chang, and Tatsuo Itoh. A 0.55 thz on-chip substrate integrated waveguide antenna. In *2018 43rd International Conference on Infrared, Millimeter, and Terahertz Waves (IRMMW-THz)*, pages 1–2. IEEE, 2018.

[61] Kirti Dhwaj, Haozhan Tian, and Tatsuo Itoh. Low-profile dual-band filtering antenna using common planar cavity. *IEEE Antennas and Wireless Propagation Letters*, 2018.

[62] Kirti Dhwaj, Lijun Jiang, and Tatsuo Itoh. Dual-band filtering antenna with novel transmission zero characteristics. *IEEE Antennas and Wireless Propagation Letters*, 2018.

[63] Nikolaos Grigoropoulos, Benito Sanz-Izquierdo, and Paul R Young. Substrate integrated folded waveguides (sifw) and filters. *IEEE Microwave and Wireless Components Letters*, 15(12):829–831, 2005.

[64] Yuanqing Wang, Wei Hong, Yuandan Dong, Bing Liu, Hong Jun Tang, Jixin Chen, Xiaoxin Yin, and Ke Wu. Half mode substrate integrated waveguide (hmsiw) bandpass filter. *IEEE Microwave and Wireless Components Letters*, 17(4):265–267, 2007.

[65] Cheng Tao, Mohammad Memarian, and Tatsuo Itoh. A metasurface assisted half-mode leaky waveguide. In *European Microwave Conference (EuMC), 2017 47th*, pages 779–782. IEEE, 2017.

[66] Ke Wu. Slow wave structures. *Encyclopedia of RF and Microwave Engineering*, 2005.

[67] Yasuo Morimoto, Amogh Waghmare, Kirti Dhwaj, and Tatsuo Itoh. A compact branch line coupler using novel periodically grounded slow-wave structure. In *Microwave Symposium (IMS), 2016 IEEE MTT-S International*, pages 1–3. IEEE, 2016.

[68] Fei-Ran Yang, Yongxi Qian, Roberto Coccioli, and Tatsuo Itoh. A novel low-loss slow-wave microstrip structure. *IEEE Microwave and Guided Wave Letters*, 8(11):372–374, 1998.

[69] Young Rack Kwon, Vincent M Hietala, and Keith S Champlin. Quasi-tem analysis of" slow-wave" mode propagation on coplanar microstructure mis transmission lines. *IEEE transactions on microwave theory and techniques*, 35(6):545–551, 1987.

[70] Alejandro Niembro-Martin, Victoria Nasserddine, Emmanuel Pistono, Hamza Issa, Anne-Laure Franc, Tan-Phu Vuong, and Philippe Ferrari. Slow-wave substrate integrated waveguide. *IEEE Transactions on microwave theory and techniques*, 62(8): 1625–1633, 2014.

[71] Haiyan Jin, Kuangda Wang, Jiapin Guo, Shuai Ding, and Ke Wu. Slow-wave effect of substrate integrated waveguide patterned with microstrip polyline. *IEEE Transactions on Microwave Theory and Techniques*, 64(6):1717–1726, 2016.

[72] Haiyan Jin, Yuliang Zhou, Yong Mao Huang, and Ke Wu. Slow-wave propagation properties of substrate integrated waveguide based on anisotropic artificial material. *IEEE Transactions on Antennas and Propagation*, 65(9):4676–4683, 2017.

[73] Daisong Zhang. Flexible rf coil array system utilizing electro-textiles for 3t mri carotid artery imaging. In *Antennas and Propagation & USNC/URSI National Radio Science Meeting, 2017 IEEE International Symposium on*, pages 1015–1016. IEEE, 2017.

[74] Daisong Zhang and Yahya Rahmat-Samii. Integration of electro-textile rf coil array with magnetic resonance imaging (mri) system: Design strategies and characterization

methods. In *2018 International Workshop on Antenna Technology (iWAT)*, pages 1–3. IEEE, 2018.

[75] Daisong Zhang and Yahya Rahmat-Samii. An ergonomie design for 3tesla mri neck coil. In *Antennas and Propagation (APSURSI), 2016 IEEE International Symposium on*, pages 463–464. IEEE, 2016.

[76] Lingnan Song and Yahya Rahmat-Samii. A systematic investigation of rectangular patch antenna bending effects for wearable applications. *IEEE Transactions on Antennas and Propagation*, 66(5):2219–2228, 2018.

[77] Daisong Zhang and Yahya Rahmat-Samii. Electro-textiles as potential candidate of flexible mri rf coil for stroke prevention. In *Radio Science Meeting (USNC-URSI NRSM), 2017 United States National Committee of URSI National*, pages 1–2. IEEE, 2017.

[78] Yasuo Morimoto, Mohammad Memarian, Xiaoqiang Li, and Tatsuo Itoh. Open-end microstrip line terminations using lossy gray-scale inkjet printing. *IEEE Transactions on Microwave Theory and Techniques*, 65(12):4861–4870, 2017.